The International Journal of Advanced Manufacturing Technology (2023) 125:5519–5540
https://doi.org/10.1007/s00170-023-11015-x

ORIGINAL ARTICLE

Preliminary results for a data-driven uncertainty quantification framework in wire + arc additive manufacturing using bead-on-plate studies

Junhee Lee[1] · Sainand Jadhav[2] · Duck Bong Kim[3] · Kwanghee Ko[1]

Received: 2 October 2022 / Accepted: 27 January 2023 / Published online: 16 February 2023

Abstract
This paper presents the uncertainty quantification (UQ) framework with a data-driven approach using experimental data in wire + arc additive manufacturing (WAAM). This framework consists of four steps. First, the experimental data, including process parameters and signatures, are obtained by performing tests in various conditions. Next, the model is constructed by surrogate modeling or a machine learning algorithm using the obtained data. Then, the uncertainties in a quantity of interest (QoI), such as bead geometry, surface roughness, microstructure, or mechanical properties, are quantified. Lastly, the UQ is verified and validated using the experimental data. The proposed framework is demonstrated with the data-driven UQ of the bead geometry on the bead-on-plate in gas tungsten arc welding (GTAW)-based WAAM. In this case study, the uncertainty sources are process parameters and signatures, and the QoI is bead geometry. The process parameters are wire feed rate (WFR), travel speed (TS), and current, while the process signatures are voltage-related features. The bead geometry includes the width and height of single-layer single bead. The results of the case study has revealed that (1) verifying and validating the data-driven UQ of bead geometry with the normal beads is conducted, and the predicted values are within the 99% confidence intervals, (2) the bead width is negatively correlated with TS, and (3) the bead height has a positive and negative correlation with WFR and TS, respectively.

Keywords Additive manufacturing · Data-driven modeling · Uncertainty quantification · Wire + arc additive manufacturing

1 Introduction

Uncertainty quantification (UQ) aims to describe the distribution of the outputs from a model using statistical metrics to analyze the effect of uncertainty sources on the variations of quantities of interest (QoIs) [1]. There are two types of sources: aleatory and epistemic. Aleatory uncertainty comes from the natural variabilities and is categorized into homoscedastic and heteroscedastic. The homoscedastic type remains the same regardless of the inputs, while heteroscedastic varies depending on the inputs [2]. Epistemic uncertainty originates from the lack of knowledge and is categorized into data uncertainty (limited or imprecise measurement) and model uncertainty (assumptions, simplifications, and numerical discretization). The model uncertainty is classified into a model form, solution approximation, or model parameter [3]. The assumptions and simplification in simulations cause the model form uncertainty, while the numerical discretization, reduced-order modeling, and an approximated solution method in simulations cause the solution approximation uncertainty [3]. In the cases of manufacturing processes, the uncertainties should be quantified since they significantly influence the process repeatability and part reproducibility [4].

UQ study can be categorized into physic-based [5, 6], physics-informed data-driven [7–9], and data-driven [10–13]. Physics-based UQ has a basis on physical laws and does not need a large amount of data and is physically accurate, but for complex processes such as additive

✉ Kwanghee Ko
khko@gist.ac.kr

1 School of Mechanical Engineering, Gwangju Institute of Science and Technology, Gwangju 61005, Republic of Korea

2 Department of Mechanical Engineering, Tennessee Technological University, Cookeville, TN 38505, USA

3 Department of Manufacturing and Engineering Technology, Tennessee Technological University, Cookeville, TN 38505, USA

manufacturing (AM), there is insufficient understanding of the underlying physics, and simplification is required. In addition, it needs calibration by experimental observation, which is computationally expensive [6, 8, 10]. Physics-informed data-driven UQ integrates physics knowledge and data and is time-saving and cost-effective because it is based on computer simulations [8, 10]. But, it does not provide the methodology for the validation because the simulation itself cannot represent the actual process. Data-driven UQ can reduce the uncertainties originating from inaccurate knowledge and the computational model [14]. Also, it can easily find the optimized process parameters for the desired properties of parts if the data are sufficient [15]. However, the accuracy of the data-driven model highly depends on the data integrity used for constructing the model [6].

Meanwhile, AM technology is used to overcome traditional subtractive manufacturing limitations with the benefits of lead time reduction, the ability to fabricate complicated geometries, and having a low buy-to-fly (BTF) ratio [16]. For example, the BTF ratio in AM is about 1.5, while it reaches 11 for subtractive manufacturing [17]. Despite these benefits, due to several tens of process parameters in AM and its inherent variabilities, poor process repeatability and part reproducibility [18, 19] are inevitable, and it is challenging to establish the design rule and the relation between the process-structure–property-performance (PSPP) [20–22]. These issues affect product reliability, business reputation, and profitability [23].

To overcome these problems, metal AM community has been focusing on process monitoring and control with uncertainty consideration [24, 25]. Since metal AM processes require time-consuming and cost-intensive data acquisition tasks for the model development and validations, research groups prefer physics-based and physics-informed machine learning-based approaches for modeling or understanding underlying physics [26, 27]. In contrast, the real experimental data obtained from metal AM, also called data-driven, has a number of benefits. First, unlike other approaches in which verification and validation (V&V) are highly challenging, the process signature and the data acquired can be used to verify and validate the model [28]. Second, this approach obtains a reliable confidence interval of the process. However, knowledge and methodology of data-driven UQ in metal AM is significantly lacking, especially based on the real-time process parameters and signatures.

Especially wire + arc additive manufacturing (WAAM) is receiving attention among metal AM processes because it has a high deposition rate, efficient usage of materials, and low production cost compared to other metal AM processes [29]. WAAM is similar to the welding process; it utilizes an arc as a heat source for melting metal wires, produces a layer consisting of continuously connected weld beads, and stacks the layers one by one. Three arcs are commonly used for heat sources: gas metal arc, gas tungsten arc, and plasma arc [30]. The gas metal arc welding (GMAW)-based WAAM uses the metal wire as a consumable electrode, meaning that there is a metal wire inside a welding torch. Therefore, it enables the mechanic system simple. That's why GMAW-based WAAM has been used for path planning and optimization [31–33]. On the other hand, the gas tungsten arc welding (GTAW)-based and plasma arc welding (PAW)-based WAAM has an external wire feeding system with a non-consumable electrode. The gas tungsten arc is conical-shaped and can be applied to deposit large-sized structures, while the plasma arc is cylindrical-shaped and is suitable for deposition with smaller weld distortion [34]. These heat sources and wires have recently been integrated with robot arms and control units, so semi- or fully automated WAAM systems are available [34–37]. It makes researchers to get real experimental data in the WAAM process more efficiently and practically.

However, WAAM is a complicated process that has several uncertainty sources [10]. The quality of the deposited parts often exhibits significant variability for the same manufacturing types, materials, and parameters, which is a considerable hindrance to widespread adoption [38]. Because of this variability, both the repeatability of the processes and the reproducibility of high-quality products have difficulties [39]. In addition, this limits the production of accurate and reliable WAAM components. Thus, understanding the uncertainty sources and their impact on the process and product quality is required to achieve quality control of WAAM processes through UQ.

Like this, WAAM processes are difficult to be modeled analytically since the process parameters accompany uncertainties and the deposited parts have unexpected variability [16]. In that point, the data-driven approach is suitable for the process repeatability and product integrity in WAAM. Integrating a data-driven approach and WAAM leads to the connection between the input parameter process and the output product quality, helping users optimize the process, make decisions, and select cost-effective materials [40]. That is why the data-driven approach is essential for establishing a process-property relation, optimizing the tool path, and carrying out accurate and stable in-situ monitoring in the WAAM process.

In this paper, we propose a data-driven UQ framework for WAAM, which consists of four steps: data acquisition, data-driven model construction, uncertainty quantification, and verification and validation. As a case study, the UQ of bead geometry in WAAM is investigated. The V&V showed that the predicted values for bead height and width are successfully predicted in a 99% confidence interval, and the sensitivity analysis revealed the correlation between the process parameters/signatures and the bead geometry. This paper is organized as follows. In Section 2, the proposed framework for the data-driven UQ framework for WAAM is explained. In Section 3, the UQ of bead geometry in GTAW-based WAAM will be presented as the case study of the proposed framework for data-driven UQ. Section 4 will discuss the issues in more detail, and the conclusion is provided in Section 5.

2 Data-driven uncertainty quantification for wire + arc additive manufacturing

A UQ framework for WAAM using a data-driven approach is proposed, as shown in Fig. 1. It has four steps: (1) data acquisition, where the process parameter and the real-time process signatures are collected for the subsequent steps; (2) data-driven model construction, where surrogate or neural network-based models are created using the acquired data; (3) uncertainty quantification and establishment of confidence intervals; and (4) verification and validation, where errors are detected, efforts are made to correct them and decide whether the mathematical model can accurately predict the actual process. Each step will be explained in detail as follows.

2.1 Data acquisition

The first step for data-driven UQ is to get data during WAAM processes. The data can be collected via computer simulation or real experiments, but real-time process signatures can only be measured by real experiments. This data will be critical in analyzing the faults' formation and propagation as the layers are stacked. The accuracy of the UQ is highly dependent on the availability of reliable data, which is hampered by the unpredictability and inherent uncertainties in the WAAM. There are a considerable number of parameters in the WAAM processes: wire feed rate (WFR), travel speed (TS), torch angle, the diameter of electrode or wire, stick-out, the distance between torch and substrate, substrate thickness, temperature, arc power, arc length, arc spread, arc rotation, welding current, welding voltage, pulse frequency, shielding gas pressure or flow rate, and proportion of mixed flux [25, 31, 41–44]. They can be measured as signatures in real time during the process (i.e., process signatures). For example, WFR can be measured via encoders, TS via accelerometers, the distance between torch and substrate via ultrasonic sensors, and the temperature via thermocouples or thermal image video cameras. The arc-related parameters, such as length, spread, and rotation, are measured by high-speed cameras. In addition, the physics-related parameters, such as specific heat, and density, are the unique characteristics of materials. They are assumed to be distributed around specific values and are commonly considered uncertainty sources.

The QoIs in WAAM are the bead geometry, surface roughness, microstructure, and mechanical properties. The QoI-related elements for bead geometry are the bead width and height, toe angles, and the penetrated depth (also called melt-through depth) [25, 44–47]. Those for surface roughness can be average roughness, quadratic average roughness, maximum valley depth, reduced valley depth, maximum peak height, reduced dale height, maximum peak to valley height, surface skewness, surface kurtosis, and wall symmetry [44]. Those for microstructure are the compositions, phases, and grain morphology (e.g., grain size, and aspect ratio) [10, 14, 39, 48]. Those of mechanical properties are tensile strength, compression strength, elasticity, elastic modulus, hardness, fracture toughness, brittleness, stiffness, ductility, fatigue, and creep [10, 39, 49].

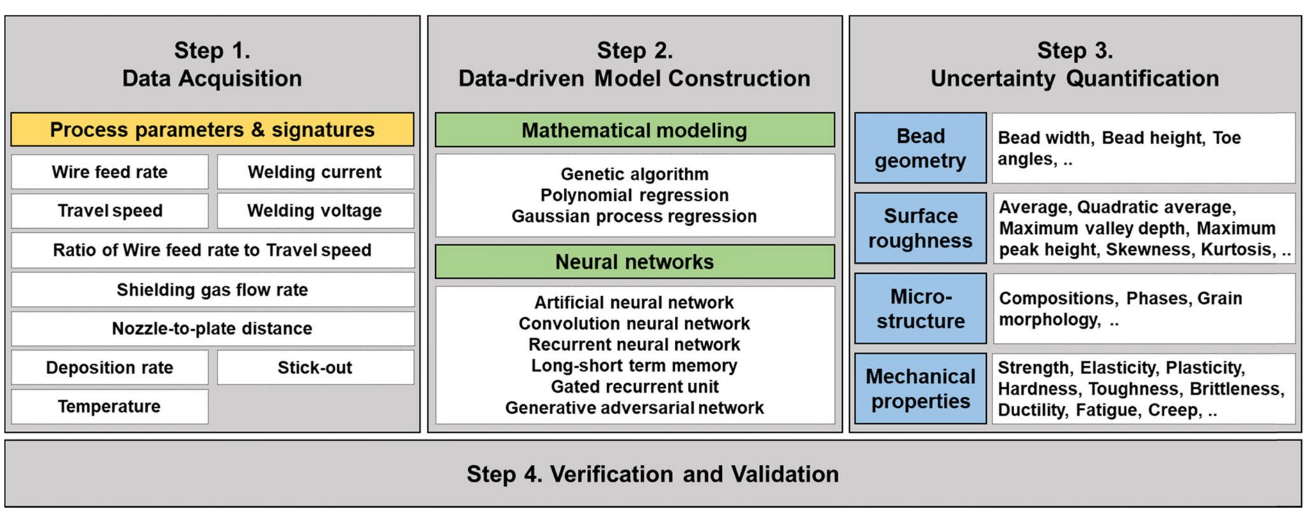

Fig. 1 Schematic workflow of data-driven UQ for WAAM

The QoIs are correlated to each other in terms of the process parameters. The bead geometry (e.g., the bead width and height, toe angles, and penetrated depth) can be correlated to surface roughness and mechanical properties. The surface roughness (R) on the deposited surface of a part is defined as the sum of the distances from the surface points to a fitted plane ($\sum d_i$) divided by the number of the surface points (N) [50]. Here, the surface points represent the outer shape of a bead, which can be captured by the bead width, height, and toe angle. Therefore, the bead geometry is directly related to the surface roughness. It is affected by the process parameters such as the WFR, TS, and so on. So is surface roughness. For a single-layer single bead (bead track), the variations of the bead width, height, and toe angles during the WAAM process are directly related to the roughness along the length of the bead tracks. The larger the variations are, the rougher the surface of the bead track is. The bead tracks with high roughness are not suitable for WAAM applications. Among the process parameters in WAAM, the arc current is known as the significant parameter that affects the roughness of the bead tracks [46]. For a multi-layer single-bead (thin wall) case, the bead width and toe angles are directly related to the surface roughness. The roughness increases as the bead height and toe angles increase when the wire feed rate increases [51]. Also, when the travel speed increases, it decreases up to a certain value and increases slightly. It is noted that the bead width and the penetrated depth decrease and the toe angles increase at that time. For single-layer multi-beads (thin plate), rather than the wire feed rate and travel, the distance between the centers of adjacent beads is a dominant factor for surface roughness [50]. The center distance in a thin plate, also called the overlapping distance, has the same role as the bead height in a thin wall case. To generate the smoothest surface, the center distance can be optimized until the area of the valley equals the overlapping area among the adjacent beads [41]. It is revealed that 0.738 of the bead width is a critical distance between the beads for the least rough surface of a thin plate.

The mechanical properties (e.g., hardness, yield strength, tensile strength, ductility, and elongation) of the thin wall are also affected by the process parameters. In this case, the ratio of wire feed rate to travel speed (RWT) is a significant parameter. RWT can be increased by reducing the travel speed or enhancing the wire feed rate. It is noted that the travel speed has more influence on RWT than the wire feed rate. If RWT increases, then heat input also increases. The heat is accumulated in the deposited parts, which makes the cooling rate slow. The slow cooling rate eventually decreases the martensite content and increases the ferrite content in the deposited parts. Therefore, the hardness, yield strength, and tensile strength decrease, but ductility and elongation increase [52]. Taken together, the increased bead width, penetrated depth and decreased toe angles by the reduced travel speed, as well as the increased bead height and toe angles by the enhanced wire feed rate, can be correlated to the decreased hardness, yield strength, and tensile strength as well as the increased ductility and elongation. In the case of multi-layer multi-beads (thick wall), the center distance between two weld beads has an effect on the mechanical properties [41, 42]. If the horizontal center distance decreases where the bead width is constant, more weld beads are needed for the desired width of the deposited part. It means that the deposited part with more weld beads is heated more frequently during the deposition. Compared to the deposited part with fewer weld beads, the cooling rate and temperature gradient of the deposited part with more weld beads decrease, so its hardness also decreases. For the same reason, the yield strength and tensile strength decrease as the center distance between weld beads reduces, while the elongation and ductility are reported to increase [53].

The QoI-related elements can be obtained during or after the WAAM process using data-driven approaches. For example, the bead geometry- and surface roughness-related elements can be measured using line scanners attached near the torch during the WAAM process or a coordinate measurement machine (CMM) after the process. Especially the width and length of a melt pool can be captured on a real-time basis using image processing techniques with a high-dynamic range (HDR) or a thermal camera, as shown in Fig. 2. The camera is attached to a welding robot arm and captures a melt pool. If it is configured as in Fig. 2a in the traveling direction, then images, as shown in Fig. 2b, will be obtained. In this case, the melt pool width is the main element to be measured. If the camera is set as in Fig. 2c in a way perpendicular to the traveling direction, then an image as Fig. 2d will be captured. In this case, the melt pool length is the main element to be measured. The melt pool width is the same as the width of the bead shape since the melt pool solidifies into a bead. So, the camera is commonly set as in Fig. 2c, and the melt pool length is obtained as shown in Fig. 2e. The melt pool depth can be captured in the simulation-based approach using finite element analysis with thermal surrogate models. However, it is not possible to measure the melt pool depth in the experiment-based approach since there is no means to monitor the inside of the substrate in real-time. The porosity can be captured by calculating the area of cavities in the region of interest of an image on a real-time basis during the WAAM process [54]. Only after the WAAM process is finished the microstructure-related properties can be obtained via microscopes such as an optical microscope, a scanning electron microscope, or energy-dispersive X-ray spectroscopy by cutting the cross-section of the deposited beads or thin/thick walls of metal alloys (i.e., destructive evaluation) [35]. The mechanical property-related ones are also obtained in tension, compression,

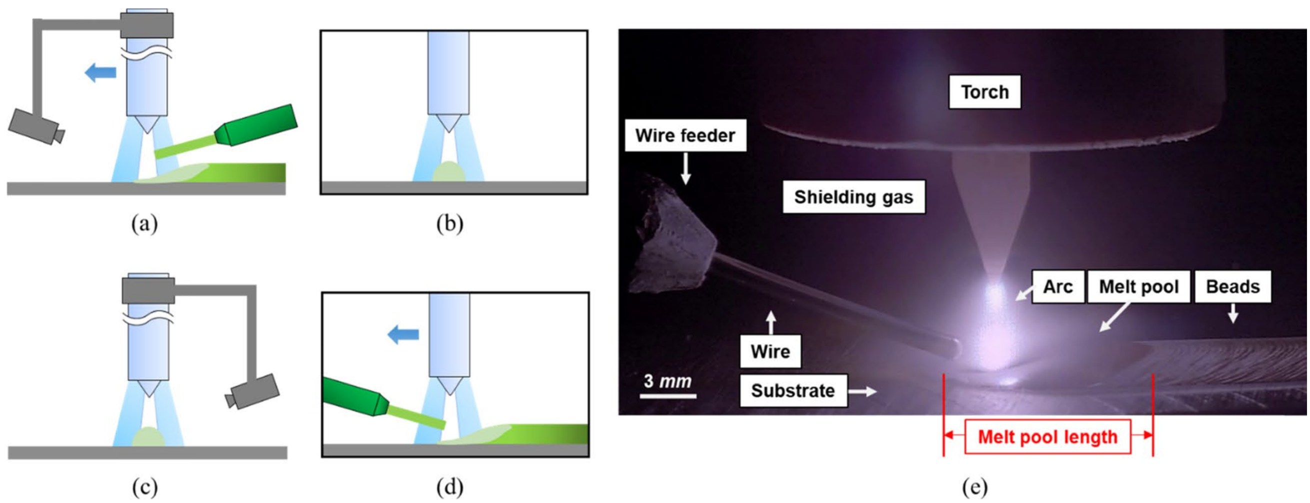

Fig. 2 Illustrations of the experimental setup to capture the melt pool width and length. **a** A camera setup in the traveling direction (a blue arrow) in case of back-feeding, **b** an example of the captured image for (**a**), **c** a camera setup perpendicular to the traveling direction in case of front-feeding, **d** an example of the captured image for (**c**), and **e** a captured image from a high-dynamic-range camera to obtain the melt pool length for (**c**)

fatigue, and creep tests using test machines after the multi-layer deposition and the precision cutting.

2.2 Data-driven model construction

For data-driven models, there are two options. One is mathematical surrogate models, and the other is neural network models. Both can present data-driven models for simulation-based and experiment-based approaches. Two review papers [40, 55] provide references for more information for those who are interested. This paper focuses on data-driven models with an experiment-based approach.

The data-driven model can be implemented using mathematical surrogate models. The mathematical surrogate models can be of three different kinds [55]. (1) Genetic algorithm is a method that mimics biological evolution to solve constrained or unconstrained optimization problems [56]. It can help solve complex issues such as nonlinear and nonconvex problems in WAAM [57]. (2) Polynomial regression uses the polynomial functions for regression problems. It can express the nonlinear relation between the input variables and the output response of QoIs in WAAM using n-th degree polynomials. And (3) Gaussian process regression is a powerful technique to approximate the distribution of regression functions and estimate the uncertainty.

The data-driven models can be built using neural network models in six different types. (1) Artificial neural network (ANN) consists of an input layer, hidden layers, and an output layer with fully connected neurons. (2) Convolution neural network (CNN) is an image-based algorithm that retains the spatial information of the image data and detects features by comparing the neighboring image data [58]. (3) Recurrent neural network (RNN) processes sequential data, such as time series process signatures through recursive loops. However, RNNs have a disadvantage that they cannot solve the problem of long-term dependence. For this reason, (4) long short-term memory (LSTM) has been developed to overcome the RNNs' disadvantage. By storing the information of process signatures in WAAM for a long time, it can reduce long-term dependence. (5) Gate recurrent unit (GRU) also overcomes RNNs' disadvantages, simplifying the architecture of LSTM. It is known that GRU outperforms LSTM for a small amount of data. (6) Generative adversarial network (GAN) is an image-based network consisting of a generator and a discriminator. The former generates fake data similar to real data, while the latter decides whether the data is fake or real. But it is known that GANs cannot generate high-resolution images and their learning processes are unstable. Like this, each neural network model has its limitations, so it is common to (7) combine more than two neural network models to overcome the limitations of each model for data-driven modeling [59]. In most neural network models, the designers determine the number of layers, nodes, and kernels to achieve the best performance. It is noted that the inputs to the models are process parameters, and the outputs are QoI-related elements.

2.3 Uncertainty quantification

The data-driven UQ implements big data obtained in a computer simulation or real experiments. In case the data is obtained through experiments, the UQ will be practical and reliable and V&V can be carried out using the process parameters and real-time process signatures. In addition, the histogram and the probability density functions (PDF) of uncertainty sources and QoI-related elements can be estimated. The confidence intervals of QoI-related elements and sensitivity analysis can also be carried out. For the data-driven UQ, the assumption that the sampled data distribution is Gaussian or uniform is not applicable. Instead, the PDF of experimental input parameters can be directly obtained by kernel density estimation (KDE) from the experimental data of uncertainty sources and QoI-related elements after getting their histograms. The KDE is one of the nonparametric and can estimate the PDF from the dataset [60, 61]. More details can be found in [60] and [61].

The variance for QoI varies within a certain range depending on the uncertainty sources, such as the process parameters and signatures. This range is called the confidence interval and is a measure of repeatability and reproducibility. The confidence interval is calculated using the mean and the standard deviation as follows [10, 62, 63].

$$\textit{Confidence Interval}\ (CI) = \bar{x} \pm Z\frac{s}{\sqrt{n}} = \left(\bar{x} - Z\frac{s}{\sqrt{n}}, \bar{x} + Z\frac{s}{\sqrt{n}}\right)$$

where $\bar{x}$ and s are the mean and the standard deviation, respectively, Z is the Z value determined by the confidence level, and n is the number of observations or samples. Table 1 shows the Z value according to the confidence levels such as 90%, 95, or 99%. In the data-driven UQ of WAAM, $\bar{x}$ and s can be the mean and standard deviation of the QoI-related elements from bead geometry, surface roughness, microstructures, or mechanical properties.

After quantifying uncertainties, the sensitivity analysis will be performed by obtaining the confidence interval with the confidence levels. It quantifies the contribution of each variable (X) to variance $\mathbb{V}(Y)$ of QoI (Y) of the model [39, 64]. The analysis can be local sensitivity analysis (LSA) or global sensitivity analysis (GSA) [65]. In this paper, the GSA is only concerned. There are two indices, which are the first-order Sobol index (also called the main effect sensitivity index, I) and the total effect Sobol index (also called the total effect sensitivity index, T) [65–67]. The first-order Sobol index is defined as

$$S_i^I = \frac{\mathbb{V}_{X_i}(\mathbb{E}_{X_{\sim i}}(Y|X_i))}{\mathbb{V}(Y)}$$

where $\mathbb{E}$ and $\mathbb{V}$ are the expected value and the variance, respectively, X_i is the i-th variable, $X_{\sim i}$ is a vector, array, or matrix of variables except X_i, and $\mathbb{E}_{X_{\sim i}}(Y|X_i)$ is the expected value of Y over $X_{\sim i}$ with X_i fixed [39, 68]. Even though the first-order Sobol index of X_i is small, it does not mean that the variable X_i has a small contribution to Y [64]. That is why the other index should also be considered together. The total effects Sobol index is defined as

$$S_i^T = 1 - \frac{\mathbb{V}_{X_{\sim i}}(\mathbb{E}_{X_i}(Y|X_{\sim i}))}{\mathbb{V}(Y)} = \frac{\mathbb{E}_{X_{\sim i}}(\mathbb{V}_{X_i}(Y|X_{\sim i}))}{\mathbb{V}(Y)}$$

where $\mathbb{E}_{X_i}(Y|X_{\sim i})$ and $\mathbb{V}_{X_i}(Y|X_{\sim i})$ are the expected value and the variance of Y over X_i with $X_{\sim i}$ fixed, respectively [66–69].

2.4 Verification and validation

The definition of V&V has been developed since 1970s, passing through hands of Schlesinger, Institute of Electrical and Electronics Engineers (IEEE), Department of Defense (DoD), American Institute of Aeronautics and Astronautics (AIAA), and American Society of Mechanical Engineers (ASME) [70]. According to the most recent definition, verification is the detection and correction of errors caused by discretization of the mathematical model during implementing the model [71, 72]. Similarly, validation is the process that determines whether the mathematical model can accurately predict the QoI-related element values [71, 73].

Previous UQ researches finished their work without V&V of UQ since it was challenging. Likewise, V&V cannot be applied to UQ directly because there is rarely technique nor method to verify and validate the uncertainty itself. However, an indirect method in data-driven approaches enables to perform V&V with using the predicted QoI-related elements from surrogate or neural network models. If the predicted QoI-related element values in testing datasets are within confidence intervals, the corresponding uncertainties from models are verified and validated. For example, the model with uncertainty predicts the QoI-related element values within the confidence intervals with a certain confidence level (e.g., 99%), and then the uncertainties are considered as being verified and validated by the model. It is the main direction that V&V of UQ pursues in this paper.

3 Implementation of data-driven uncertainty quantification for bead geometry in WAAM

As a case study, the proposed framework of data-driven UQ is applied to the bead geometry in GTAW-based WAAM in a single-layer single-bead deposition (i.e., bead track) on

Table 1 Z value and its corresponding confidence level

Confidence level	50%	80%	85%	90%	95%	99%	99.5%	99.9%
Z value	0.674	1.282	1.440	1.645	1.960	2.576	2.807	3.291

a plate considering bead width and height. There are four steps, as shown in Fig. 3. In step 1 (data acquisition), a WAAM system, including a power source, a welder, a wire feeder, and a robot arm, is set. Also, the process parameters, such as WFR, TS, current, voltage, or shielding gas flow, are determined. Then, the process signatures are recorded by a real-time measurement unit, and the deposited single-layer single-bead tracks are scanned with a CMM. The one-dimensional (1D) recording data of process signature and the 3D scanning data of bead tracks are synchronized for a database. In step 2 (data-driven model construction), the database is split into a training and a testing dataset. This step uses a training dataset for training and validating a neural network model using cross-validation. A neural network model is chosen as a data-driven model. In step 3 (uncertainty quantification), the uncertainty sources from the experimental data of the WAAM process are analyzed. Then, the uncertainty of bead geometry is quantified by calculating the confidence interval of bead geometry for a testing dataset. In step 4 (verification and validation), the model is verified and validated by the predicted bead geometry using a testing dataset with confidence intervals. Each step will be explained in Sections 3.1 to 3.4.

3.1 Step 1: data acquisition

3.1.1 WAAM system setup and process parameters

The GTAW-based WAAM process used for this research is shown in Fig. 4. It consists of a 6-axis robot arm (Fanuc Arc Mate 120iC), its controller (Fanuc R-30iA), an electric welder (Miller Dynasty 400), a wire feeder (VR7000), and a real-time voltage/current measurement unit (Miller Insight Arc Agent). The wire material is Inconel 625 (IN625) with a diameter of 1.2 mm, and the substrate material is low carbon steel (LCS) plate of five 300 × 300 × 12 mm.

In GTAW-based WAAM, the operator can set the process parameters before the process. The controllable parameters include WFR, TS, current, voltage, and shielding gas flow rate. Among them, WFR, TS, and current are considered influential process parameters. In this paper, WFR and TS

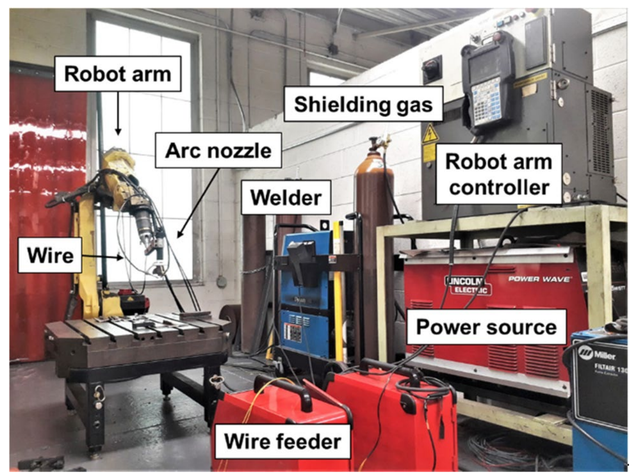

Fig. 4 GTAW-based WAAM system setup consisting of the robot arm, nozzle, welder, controller, power source, shielding gas, and wire feeder

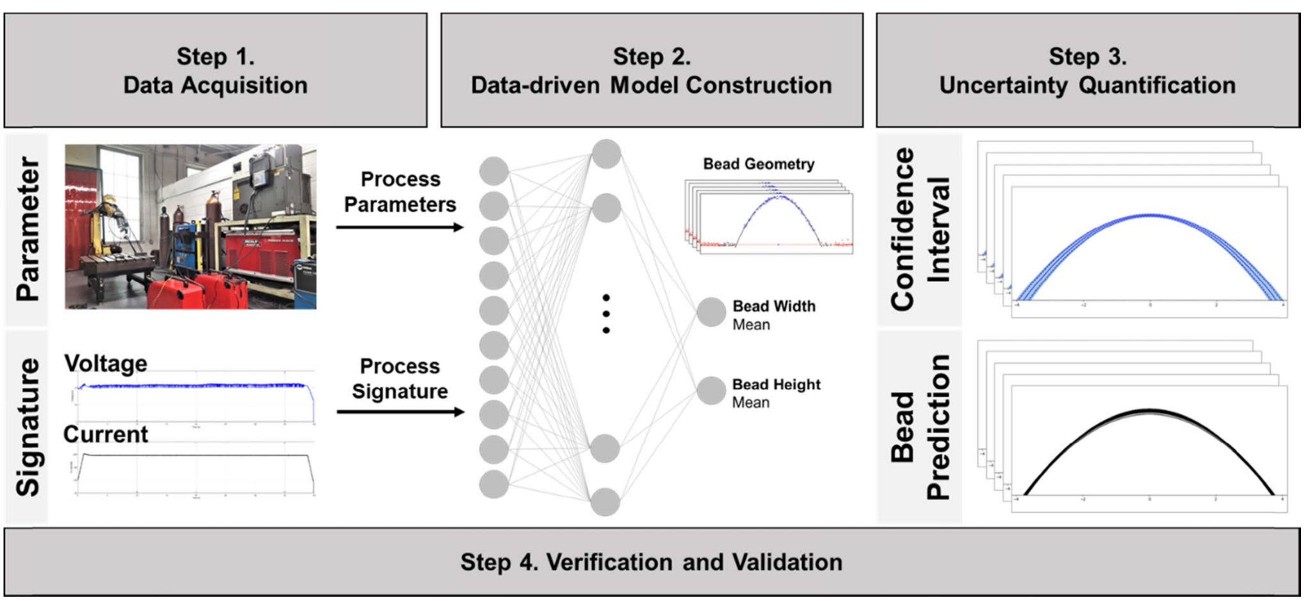

Fig. 3 Schematics of experiment-based data-driven UQ study for bead geometry in GTAW-based WAAM in four steps of data acquisition, model construction, UQ, and V&V

were changed to adjust the deposition area and deposition rate. The WFR was set at a range of 75 to 300 cm/min, incrementing by 25 cm/min, preventing a periodic protruding concave defect of beads in less than 40 cm/min. The TS was from 10 to 100 cm/min, incrementing by 10 cm/min, going through a head accumulation of less than 20 cm/min, and an undercut or concave of more than 90 cm/min. The current was kept constant at a value of 200 A, since less than 140 A would cause a poor wetting condition in the solidification of the molten pool, and more than 300 A would form a poor bead geometry because of decreasing the surface tension of the molten pool at high temperature [74]. The voltage between the tip of the arc nozzle and the substrate varies during the process even though a voltage was set as 15 V, while the current remains constant, as shown in Fig. 5. Since the varying voltage mainly affects the uncertainty of bead geometry when other process parameters, such as WFR, TS, and current, are constant, it is a parameter that should be investigated. The shielding gas was a mixture of 70% Argon and 30% Helium, and its flow rate was constant at 30 L/min. It was revealed that the shielding gas flow rate did not affect the bead geometry. In this research, the single-layer single-bead deposition was conducted with 100 combinations of process parameters with the given WFR and TS in a full factorial experimental plan. Table 2 shows the process parameters used in this study.

Table 2 Process parameters of GTAW-based WAAM

Parameters	Unit	Range
Wire feed rate (WFR)	cm/min	75 ~ 300
Travel speed (TS)	cm/min	10 ~ 100
Current	A	200
Voltage	V	15
Shielding gas flow rate	L/min	30

3.1.2 Acquisition of WAAM process signatures and data preprocessing

The process signatures are real-time output signals from the welding machine. In this study, Miller Insight Arc Agent detected and recorded the voltage and current, as shown in Fig. 5.

For the 1D signature of the GTAW-based WAAM process, seven features were extracted from a voltage as the process signatures: the mean, standard deviation, skewness, kurtosis, the absolute value of the difference between mean and maximum, between mean and minimum, and between mean and median over a period [75]. These voltage-related features were calculated during every period (e.g., period #1, #2, and #3) to form a datum within each period. The period is defined by bandwidths and intervals, as shown in Fig. 6. The bandwidth is the length of a period and is set to 1.0, 1.5, 2.0, 3.0, and 4.0 s, and the interval is the length between the present period and the next one and is set to 0.1, 0.2, 0.5, and 1.0 s. For example, if the bandwidth was 2.0 s, the interval was 0.5 s, and period #1 started at 1.0 s, then period #1 was from 1.0 s to 3.0 s, period #2 was from 1.5 s to 3.5 s, and period #3 was from 2.0 s to 4.0 s. One dataset consisted of seven voltage-related features with one bandwidth and one interval from 1D signature data of all single-layer single-bead tracks. So, twenty datasets were generated for neural network models with all combinations of five bandwidths and four intervals.

3.1.3 Acquisition of bead geometry and data preprocessing

The QoI is bead geometry, which includes the bead width and height. The bead width is the distance between two points where two fitted curves of the LCS substrate and the IN625 weld bead meet. The bead height is the distance from the fitted curve of the LCS substrate to the highest point of the IN625 bead. It is necessary to measure the bead width

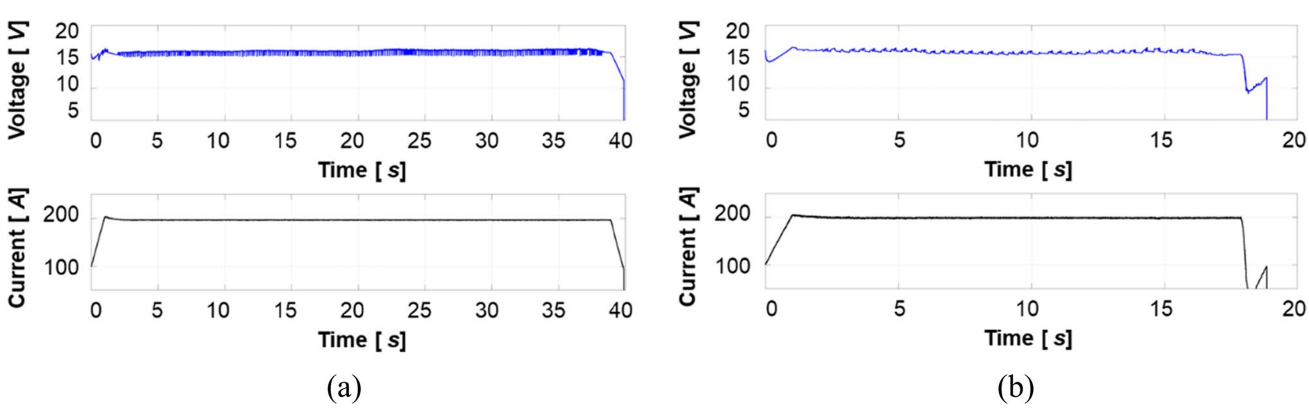

Fig. 5 1D process signatures from process parameters (voltage and current) for **a** normal and **b** abnormal single-layer single beads

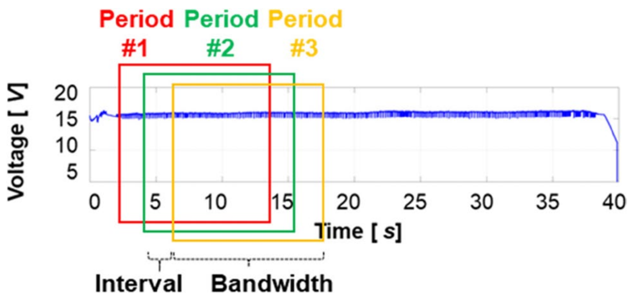

Fig. 6 Periods defined by bandwidths and intervals for 1D voltage signature

and height by cutting all single-layer single-bead tracks, but it is highly time-consuming. Therefore, laser scanning technology was used to measure the bead geometry.

After depositing single-layer single-bead tracks on substrate plates, the bead tracks were scanned using a CMM. The scanning was automatically saved as computer-aided design (CAD) files in PC-DMIS software [76], as shown in Fig. 7a, but it was necessary to convert CAD files to 3D point cloud files for further processing. Each single-layer single-bead track was segmented on CloudCompare [77]. Using the single-layer single-bead track point cloud data, the robot arm's moving direction and route were calculated by slicing the bead track normal to the moving direction. The cross-section planes were generated when slicing the bead track for projecting the points onto planes within a certain tolerance. The bead width and height were obtained on each cross-section plane by fitting the bead profile and substrate with a quadratic curve, as shown in Fig. 7b. The bead width is computed using the points where the function meets the plane defining the substrate. The bead height is computed as the maximum value of the function with respect to the plane.

Similar to the 1D voltage signature, the five bandwidths and four intervals were also applied to the 3D scanned data, as shown in Fig. 8. The distance between the cross-sections was 0.1 mm, and the number of the cross-sections was considered for each period, as shown in Table 3. The means of the bead width and height were calculated in each period. For example, if the bandwidth was 2.0 s, the interval was 0.5 s, and the travel speed was 30 cm/min, then the bead widths and heights from the 67 cross-sections were averaged to form the mean of the bead width and height for the corresponding period. One dataset consisted of the mean values of the bead width and height with one bandwidth and one interval from the 3D scanned data of all single-layer single-bead tracks. So, twenty datasets were generated for the 3D scanned data, as done for the voltage-related 1D process signature data.

3.1.4 Synchronization of process signatures and bead geometry

Matching the 1D voltage signature and the 3D CMM data was necessary. The best option is to synchronize a real-time voltage/current measurement unit with a robot arm controller, an electric welder, a wire feeder, and a CMM unit for on-site monitoring, but data processing method is more intuitive in data-driven approach. Figure 9 shows the schematic of the synchronization. The arc at the end of the welding machine was switched on and off for 1 s with respect to changing the voltage signature. The bead geometries at the start and

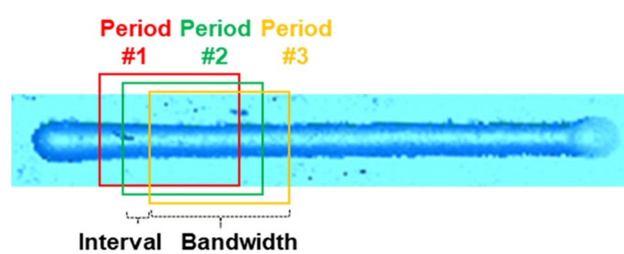

Fig. 8 Periods defined by the bandwidths and intervals for the 3D CMM point cloud in a single-layer single-bead deposition

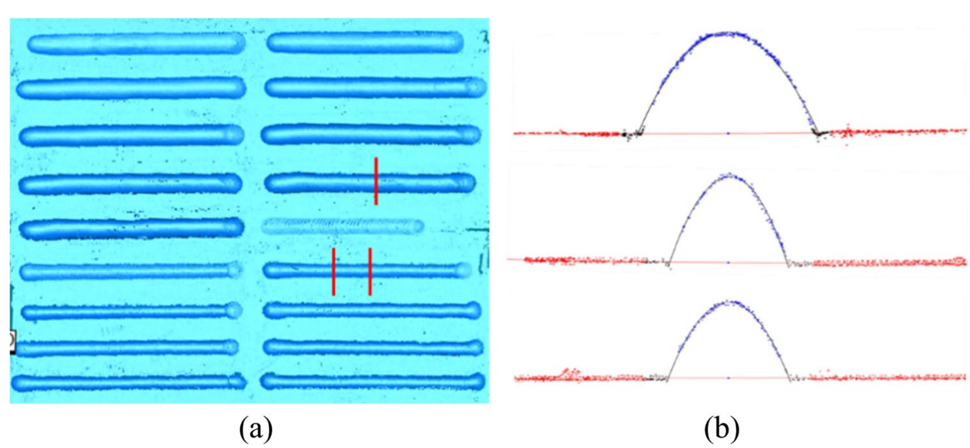

Fig. 7 Data preprocessing for obtaining the bead geometry from the point cloud scanned by a CMM. **a** The scanned data was saved as a CAD file and was converted to point clouds. **b** The bead profile was fitted to estimate the bead width and height.

Table 3 A number of cross-sections for CMM data for a period to calculate the mean of bead width and height

Bandwidth or interval [s]	Travel speed [cm/min]									
	10	20	30	40	50	60	70	80	90	100
0.1	2	3	5	7	8	10	12	13	15	17
0.2	3	7	10	13	17	20	23	27	30	33
0.5	8	17	25	33	42	50	58	67	75	83
1.0	17	33	50	67	83	100	117	133	150	167
1.5	25	50	75	100	125	150	175	200	225	250
2.0	33	67	100	133	167	200	233	267	300	333
3.0	50	100	150	200	250	300	350	400	450	500
4.0	67	133	200	267	333	400	467	533	600	667

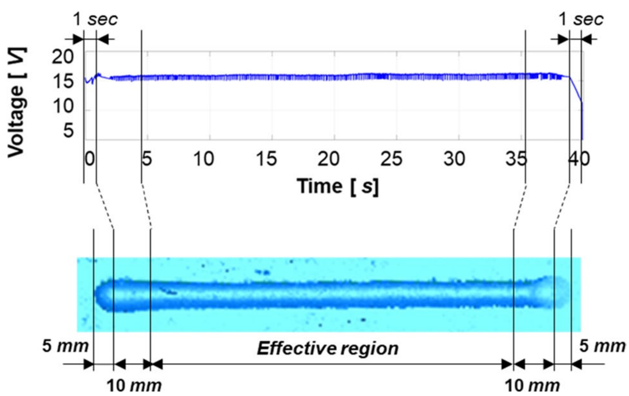

Fig. 9 Synchronization of 1D voltage signature and 3D CMM data

the endpoint of the process were unstable. Therefore, 10 mm from both ends of the bead tracks in the CMM data were excluded. The intermediate region of the bead tracks (i.e., the effective region [25]) was used for acquiring the bead geometry. The corresponding time in 1D voltage signature for the 10 mm regions from both ends of the bead tracks and the effective region from the middle of the bead tracks was calculated using the TS for synchronization.

3.2 Step 2: data-driven model construction

3.2.1 Model development

Either mathematical surrogate models or neural network models are typically used for data-driven techniques. The mathematical surrogate models are suitable for theoretical and simulation-based approaches since several physical principles such as arc physics, thermodynamics, heat transfer (e.g., conduction in beads and substrate, convection in a molten pool, and radiation from the heated deposited part), and fluid dynamics (e.g., the density and viscosity of molten pool, and their changes during cooling) can be given as mathematical equations. The variables in the equations are subjected to experimental settings such as wire/substrate materials, oxidation of materials, and ambient temperature in the WAAM process. However, it is challenging to consider all the physical principles during the experiment in the real world. On the other hand, neural network models need input and output elements regardless of complex physical principles or corresponding mathematical relations. The input can be process parameters in the real experiment, and the outputs can be elements that researchers are interested in. This modeling technique is called black-box modeling, which is commonly used for understanding the relationship between input and output experimentally. This paper focuses on the framework for quantifying the uncertainty of output elements with respect to input parameters in real experiments. Therefore, neural network models are used in this paper rather than mathematical surrogate models.

It was necessary to search for a proper neural network model for the case study of this paper. In the case study, one-dimensional (1D) process parameters and signatures are input elements. 1D means that it has data as a specific number rather than a 2D image or a 3D space coordinate. Therefore, 2D image-based neural networks (e.g., CNN, GAN) were not appropriate for this case study. The outputs are the bead width and height since the quantity of interest in the case study is bead geometry. Many research papers that concern the process parameters as input elements and the bead geometry as output have utilized an ANN as a model rather than other neural network models (e.g., RNN, LSTM, GRU) [31, 45, 78, 79]. Also, a review paper confirms that an ANN is one of the best data-driven models suitable for AM [55]. Therefore, an ANN model is utilized as a modeling technique in our paper. The architecture of the ANN is shown in Fig. 10. The inputs to the models are WFR, TS, current, and voltage-related features over a period, including mean, standard deviation, skewness, kurtosis, and the absolute difference between mean and maximum, mean and minimum, and mean and median. The outputs from the model are the mean of the bead width and the mean of the bead height.

3.2.2 Model selection

For ANN, determining the number of layers and nodes in the hidden layer was needed. When there was one hidden layer in the neural network model, the model showing the smallest loss (i.e., mean squared error (MSE)) was selected. The procedure was performed with epoch 20 and by increasing the number of nodes in the hidden layer from 1 to 250. Among these architectures, the one that has the lowest mean of loss in *k*-fold cross-validation using a training dataset where *k* is equal to 5. The neural network architecture of 10–100-2 (i.e., 10, 100, and 2 nodes in the input, hidden, and output layers, respectively) has been selected and used in this research. That is, the selected neural network architecture has the lowest mean of MSE in *k*-fold cross-validation using a training dataset. The model architecture selection was performed using a workstation with an Intel(R) Core™ i7-8700 K CPU (3.70 GHz) with 64 GB RAM and NVIDIA GeForce GTX1080 GPU using Python 3 with TensorFlow and Keras, running on the Windows 10 64-bit operating system.

3.3 Step 3: uncertainty quantification

3.3.1 Uncertainty sources

The uncertainty sources that affect the bead geometry are (1) WFR, (2) TS, (3) current, and (4) voltage. The distribution of the WFR, TS, and current of training and testing datasets are illustrated in Fig. 11a, b, and c. However, even if the user sets the voltage at a specific value as a process parameter, the actual measured value of voltage changes, which is considered the major uncertainty source. Figure 11d shows the distribution of the average voltage within the periods in the training and testing dataset. It has a similar shape to the Gaussian distribution. Similarly, Fig. 11e to j shows the distribution of voltage-related features. The standard deviation, Fig. 11e, and the absolute difference between mean and median, Fig. 11h, are similar to the exponential distribution. The absolute difference between mean and maximum, Fig. 11f, and mean and minimum, Fig. 11g, has a similar shape to the Poisson distribution. The skewness, Fig. 11i, and the kurtosis, Fig. 11j, have a similar shape to the Gaussian distribution.

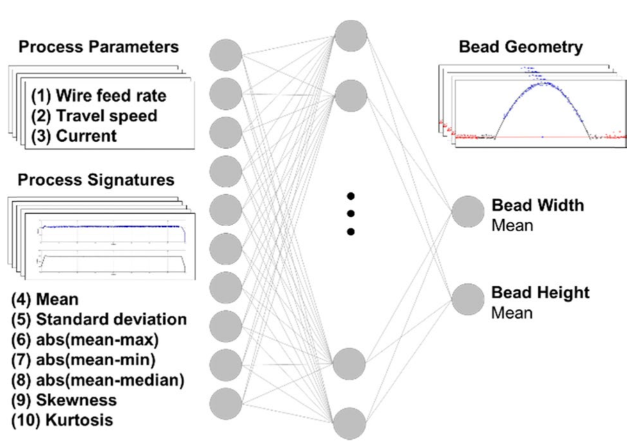

Fig. 10 The architecture, inputs, and outputs of the artificial neural network model

3.3.2 Mean and variance of the bead geometry from the experiment-based data

Table 4 describes the expected value ($\mathbb{E}$) and variance ($\mathbb{V}$) of the bead width and height for normal and abnormal bead tracks as results of the experiments with the combination of the process parameters. The normal beads #17, #26, #35, #44, and #53 are in the testing dataset, but the abnormal bead tracks are not considered testing datasets. In Table 4, the expected values, $\mathbb{E}_{bwm}$ and $\mathbb{E}_{bhm}$, are dependent on process parameters such as WFR or TS. It will be discussed in Section 4.2. The variance of bead width and height, $\mathbb{V}_{bwm}$ and $\mathbb{V}_{bhm}$ respectively, in normal bead tracks are apt to be lower than in abnormal bead tracks. It means that the normal bead tracks are more stable than the abnormal ones.

3.3.3 Confidence interval

The advantage of this approach is that it can obtain the confidence interval experimentally using the mean and variance of QoI-related elements. The QoI in this case study is the bead geometry, and the bead width and height are the QoI-related elements. Figure 12 shows the confidence interval of the bead geometry for the normal bead tracks in the testing dataset. The confidence intervals for normal bead tracks are shown as the blue regions. The dark-shaded region represents the confidence interval with a 95% confidence level, and the light-shaded region is 99%. The solid blue line in the middle shows the mean value. From the confidence intervals of each bead track, the histograms of the bead width and height and their fitted PDF curves are shown in Fig. 13. It is noted that Fig. 13 is for the bead width and height on the positive side, which is magnified in Fig. 12. That is, the values on the horizontal axis in Fig. 13a, c, e, g, and i are half of the bead width, while the values on the horizontal axis in Fig. 13b, d, f, h, and j are the bead height.

3.3.4 Global sensitivity analysis

GSA was also performed using the Sobol indices discussed in Section 2.3 with the training dataset. The objective of GSA was to analyze the influence of various uncertainty sources on the variability of bead geometry. The *SALib* [80] was used for GSA in this research. Figure 14 shows the first-order Sobol index where the uncertainty in the bead geometry came from the current.

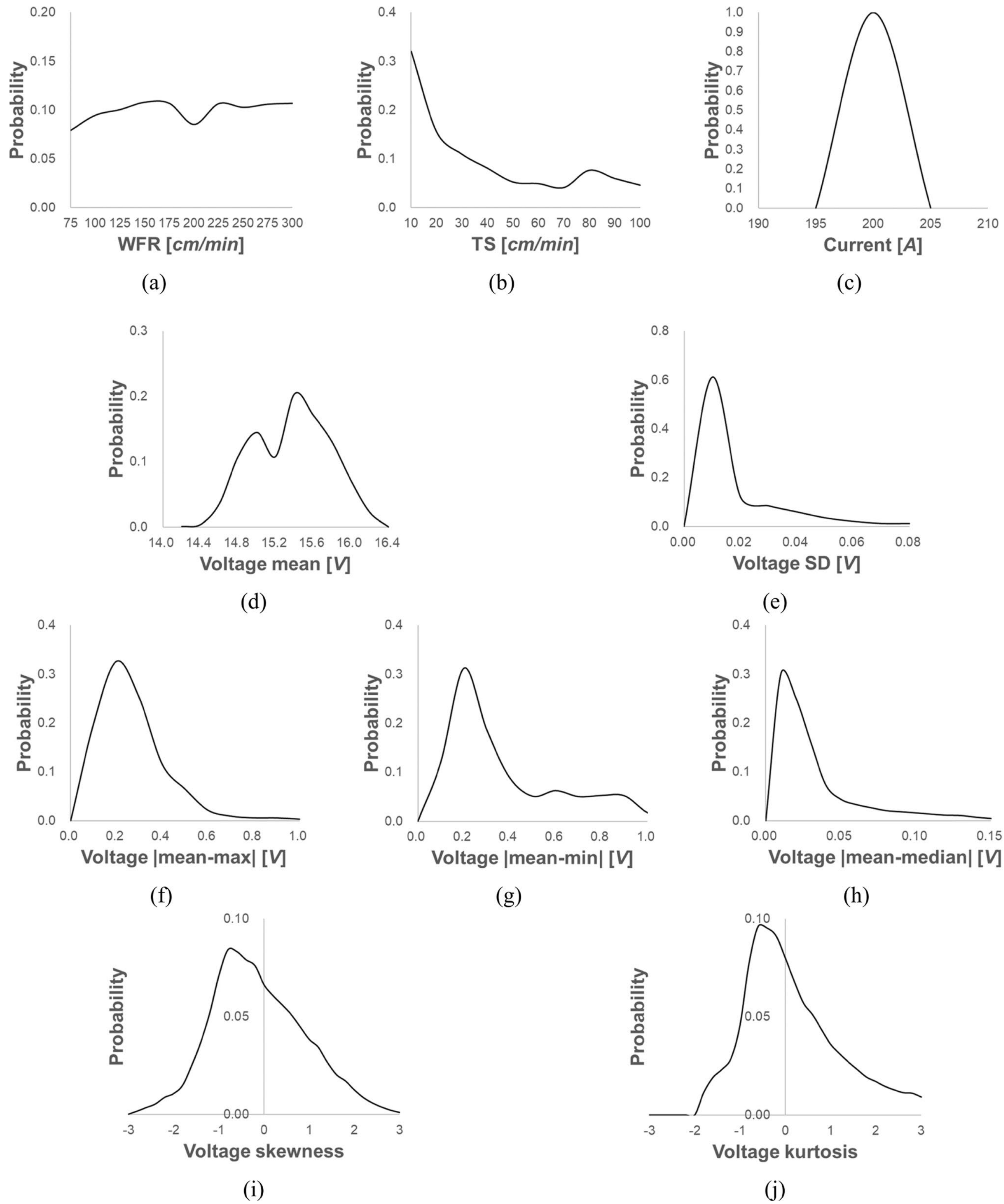

Fig. 11 Probability distribution of uncertainty sources that include the process parameters and signatures. **a** WFR, **b** TS, **c** current, and voltage-related features: **d** mean, **e** standard deviation, and the absolute difference between **f** mean and max, **g** mean and min, **h** mean and median, **i** skewness, and **j** kurtosis

Table 4 Expected value ($\mathbb{E}$) and variance ($\mathbb{V}$) of the bead width and height in the normal and abnormal tracks

Types	Bead track	WFR [cm/min]	TS [cm/min]	$\mathbb{E}_{bwm}$[mm]	$\mathbb{V}_{bwm}$[mm^2]	$\mathbb{E}_{bhm}$[mm]	$\mathbb{V}_{bhm}$[mm^2]
Normal (*testing dataset*)	#17	100	20	7.593	0.204^2	2.365	0.036^2
	#26	125	30	6.135	0.185^2	1.552	0.096^2
	#35	150	40	4.436	0.149^2	1.463	0.033^2
	#44	175	50	4.146	0.083^2	1.101	0.044^2
	#53	200	60	3.710	0.061^2	0.893	0.021^2
Abnormal	#60	200	60	4.313	0.449^2	1.966	0.197^2
	#69	225	70	3.555	0.213^2	1.627	0.110^2
	#78	250	80	3.612	0.228^2	1.392	0.066^2
	#87	275	90	2.848	0.162^2	1.700	0.328^2
	#98	300	100	3.155	0.312^2	1.303	0.088^2

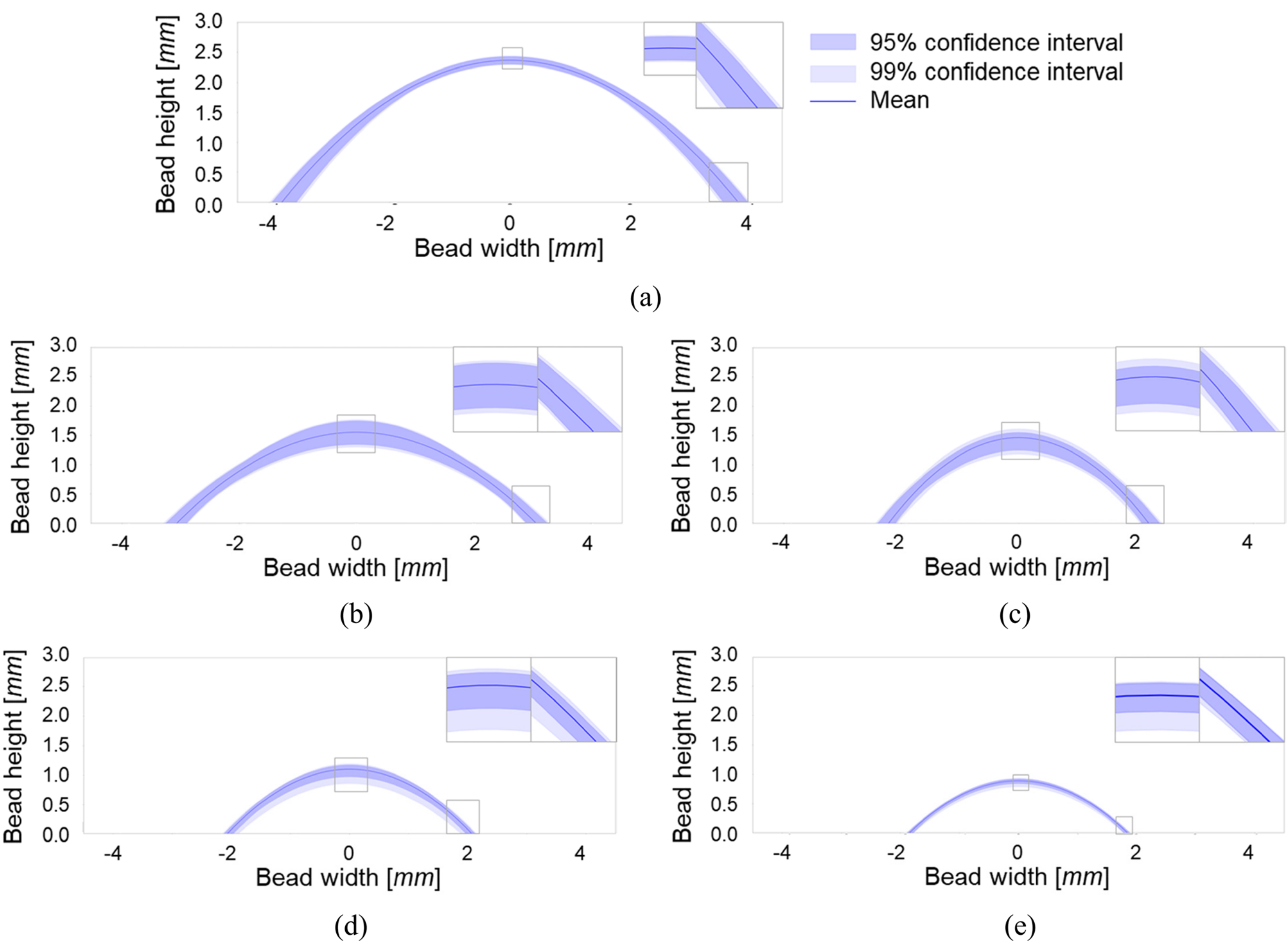

Fig. 12 Confidence intervals of the bead geometry for tracks of **a** #17, **b** #26, **c** #35, **d** #44, and **e** #53

If the current is excluded, the standard deviation of voltage affects the bead geometry. Figure 15 shows the total effect Sobol index, where the uncertainty mainly came from the WFR, followed by the kurtosis of voltage for the bead width and the standard deviation of voltage for the bead height.

3.4 Step 4: verification and validation

The bead width and height in the testing dataset were estimated. Then, the bead geometry was drawn as a quadratic equation using the estimations. Figure 16 compares the confidence intervals of bead geometry from the experiments and

Fig. 13 PDF of bead geometry for (width, height) in different experiments: **a**, **b** #17, **c**, **d** #26, **e**, **f** #35, **g**, **h** #44, and **i**, **j** #53

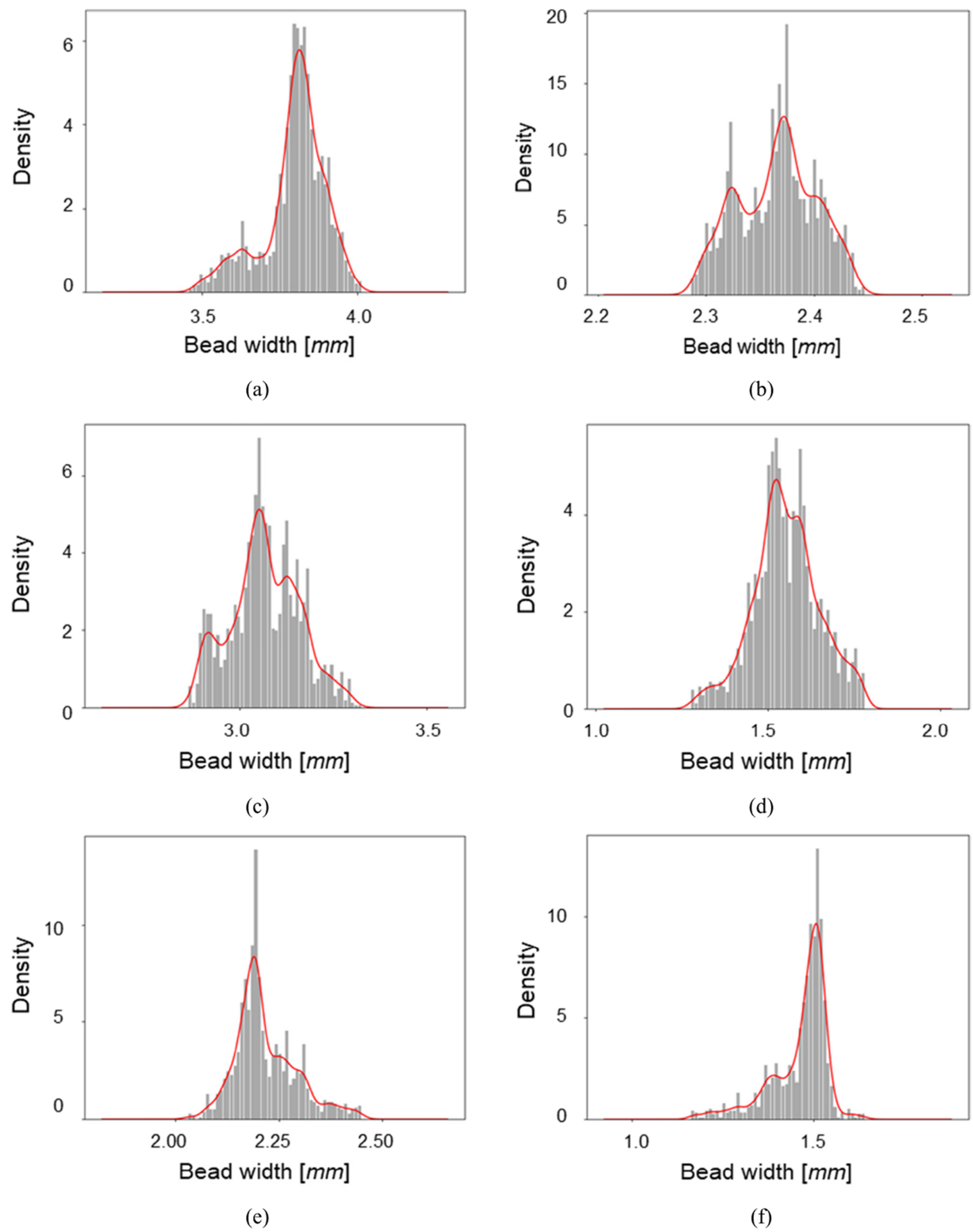

the prediction using the UQ model. It is revealed that verifying and validating the data-driven UQ of bead geometry with the normal beads is suitable since the predicted values are within the confidence intervals.

4 Discussion

4.1 Window map

As explained in Section 3.1, 100 single-layer single beads were deposited using a full factorial experimental plan by combining the process parameters, WFR and TS. The bead width and height were measured on each cross-section plane, as described in Fig. 7. Their mean and standard deviation were calculated in the reliable region. An expert decided whether a bead track was normal or abnormal. So, 100 bead tracks were classified as 54 normal and 46 abnormal; each notated as blue for normal ones and red for abnormal ones in a window map.

A window map was obtained experimentally using the mean and standard deviation of bead geometry for 100 single-layer single beads. It presents an appropriate range of the parameters to choose for a stable weld metal. The window map is drawn in the WFR-TS plane, as shown in Fig. 17. The figure describes the bead shape conditions according to the combination of WFR and TS. The blue circle presents the normal (perfect) bead shape (Fig. 18a), which can be

Fig. 13 (continued)

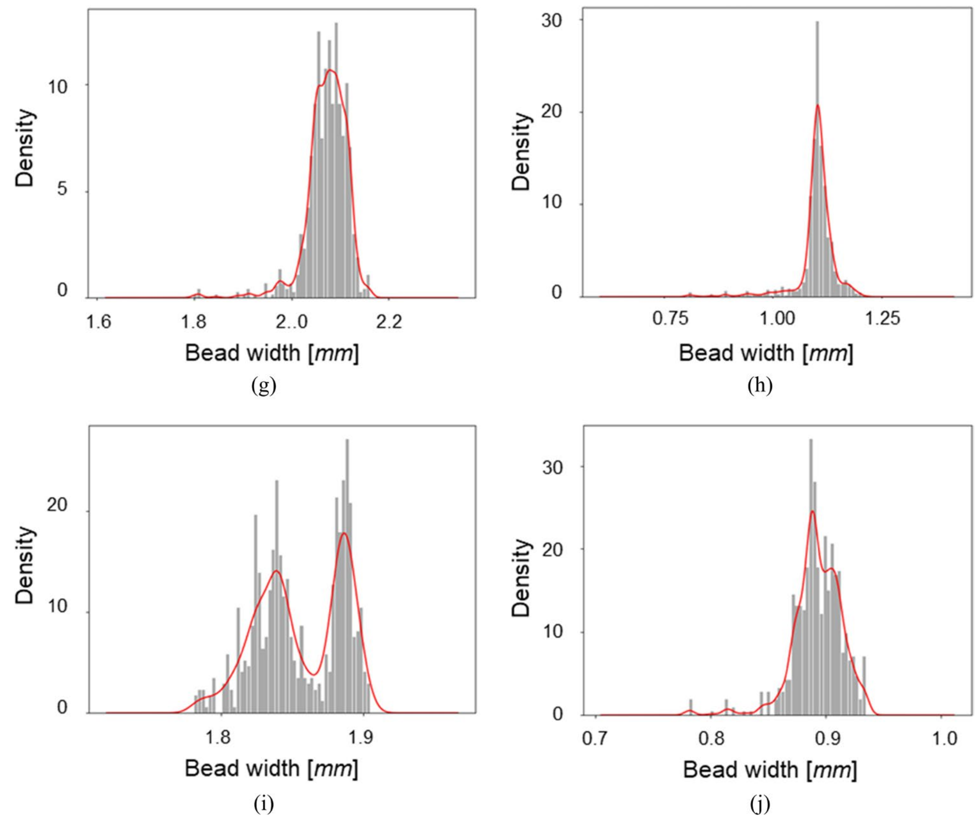

Fig. 14 First-order Sobol index of uncertainty sources on **a** bead width and **b** bead height

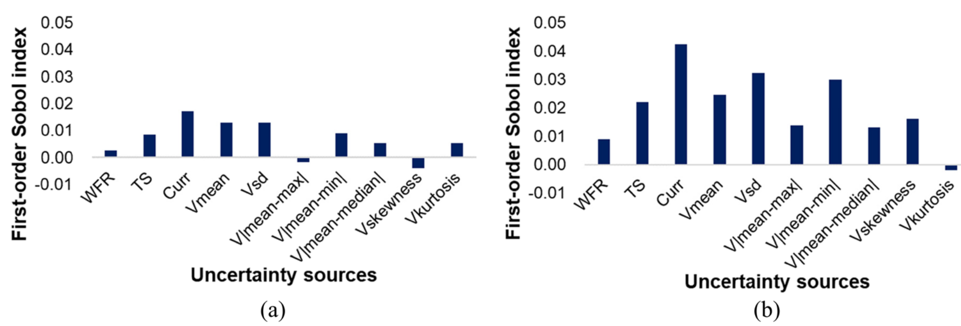

Fig. 15 Total effect Sobol index of uncertainty sources on **a** bead width and **b** bead height

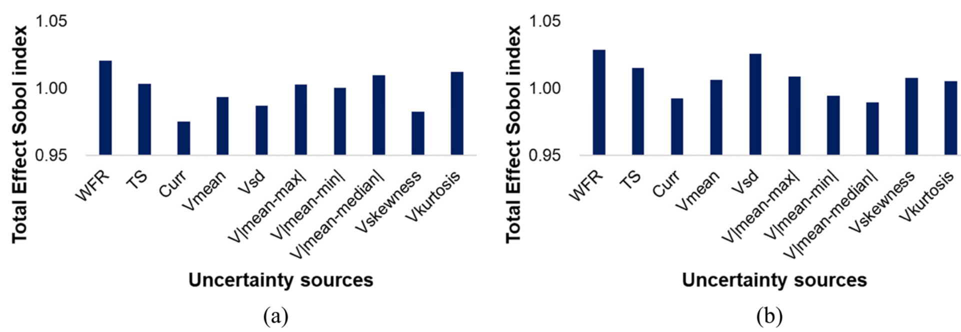

utilized in the WAAM process. The red rectangle represents the lack of fusion (Fig. 18b), which has an unmelt feed wire material on the beads since the wire feed rate is excessive or the heat input is insufficient. The red triangle denotes humping (Fig. 18c), which has an irregular bead width and height along the travel direction. It is mainly caused by the excessive travel speed compared to the wire feed rate. There is a bead shape, balling, as shown in Fig. 18d. It is a severe

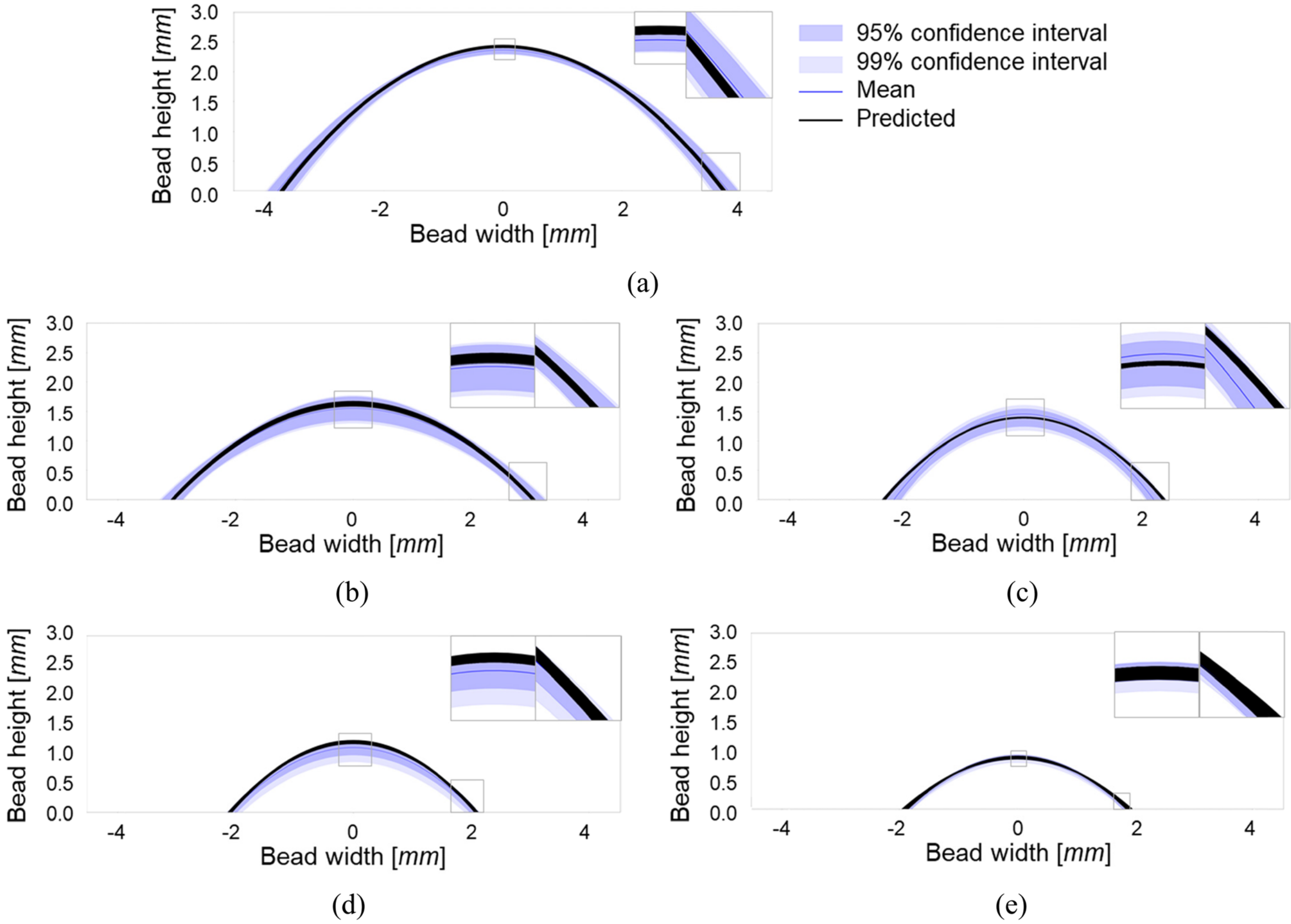

Fig. 16 Comparison of the confidence intervals (blue) obtained from testing dataset and the predicted bead geometry (black) for normal bead **a** #17, **b** #26, **c** #35, **d** #44, and **e** #53

version of humping, in which the beads are generated discontinuously, so the beads resemble balls standing in a line. The lack of fusion, humping, and balling is all considered imperfect (abnormal) beads, which cannot be used for multi-layer single-bead, single-layer multi-bead, or multi-layer multi-bead parts. Instead, only the perfect beads should be considered to predict the mechanical properties.

In addition, other window maps can be expressed in WFR-TS-BW space and WFR-TS-BH space, plotting bead width (BW), or bead height (BH) against the WFR-TS plane shown in Fig. 19. It presents how the mean of bead width and height for the IN625 single-layer single beads are generated experimentally in the real world by GTAW-based WAAM according to the combination of WFR and TS. The bead width seems more sensitive to TS than WFR, while bead height is sensitive to both. If the 3D window maps in Fig. 19 are viewed normal to BW-WFR or BH-WFR plane along the TS axis, an analysis of variance can be conducted.

4.2 Analysis of variance

The analysis of variance (ANOVA) in this case study is to figure out the effects of the process parameters, such as WFR and TS, on the bead width and height for single-layer single beads. Figure 20 shows the effect of WFR and TS on bead geometry. The bead width is not significantly affected by WFR. It remains relatively constant as the WFR increases, as shown in Fig. 20a. It is also noted that a lower TS leads to an increase in the bead width. Figure 20b shows that the bead height increases as the WFR increases. The increasing rate of bead height at TS 10 cm/min (TS 10) is the largest among those at other TSs. In other words, the lower the TS, the larger the increasing rate of bead height when the WFR increases. It is also noted that a higher TS leads to a decrease in bead height. The aspect ratio (W/H) is defined as the ratio of bead width to bead height in this paper. It significantly decreases as the WFR increases, as shown in Fig. 20c.

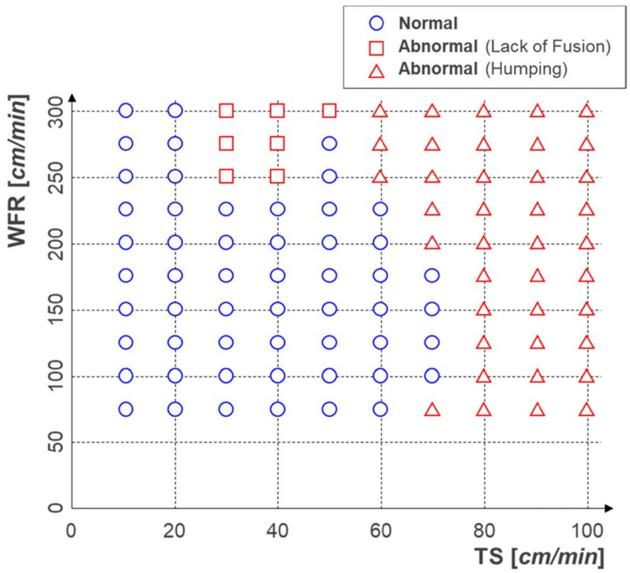

Fig. 17 Window map on WFR-TS plane for Inconel 625 GTAW-based WAAM process. Normal beads are marked as blue circles, abnormal ones for lack of fusion as red rectangles, and abnormal ones for humping as red triangles

(a)
(b)
(c)
(d)

Fig. 18 Bead shape conditions in single-layer single-bead deposition. **a** Normal (or perfect), **b** lack of fusion, **c** humping, and **d** balling

4.3 Advantages of data-driven UQ using experimental data

Data-driven UQ using experimental data has the following advantages. First, it can be verified and validated with real processes or parts, while it is a challenge in the simulation-based UQ. In the data-driven UQ, the validation can be performed using real process signatures and responses. The process parameters such as WFR, TS, current, voltage, heat source power, power distribution, layer thickness, overlapping distance, or substrate preheat [81] can be set by the operator and can be measured by sensors in a real time. Also, after manufacturing, the characteristics of parts, such as bead geometry, surface roughness, mechanical properties, electrical properties, chemical properties, or thermal properties, can be considered as responses [18].

Second, this method is more practical. Physics-based or physics-informed UQ has a lot of assumptions, so it is possible to ignore extreme cases. For example, the physics-based UQ assumes that all wire material in WAAM undergo the same melting and solidification process with constant density [8]. In the physics-informed UQ, the order of the model in a large-scale system is reduced to decrease the computational cost [9]. But, the order reduction of an original system and the assumptions for the reduced-order physics can lead to inaccuracies and uncertainties [9]. However, the data-driven UQ using the experimental data provides more reliable data [55]. Furthermore, it can provide remarkable insights by being applied to the in situ monitoring and the in situ process optimization [55].

Third, even though the PSPP relations have been established in AM process in different researches [15, 20–22, 55, 72, 82], the process-signature-structure–property-performance (PS^2P^2) relation in WAAM can be considered by the data-driven UQ using experimental data. The process parameters significantly affect the microstructure and product qualities, and the microstructure features influence the mechanical properties [15, 55]. Also, the performances such as the distortion, internal stress, and failure of parts

Fig. 19 Window map in WFR-TS-BW space and WFR-TS-BH for Inconel 625 GTAW-based WAAM process: **a** the mean of bead width and **b** bead height is fitted with a surface in terms of WFR and TS (see in color)

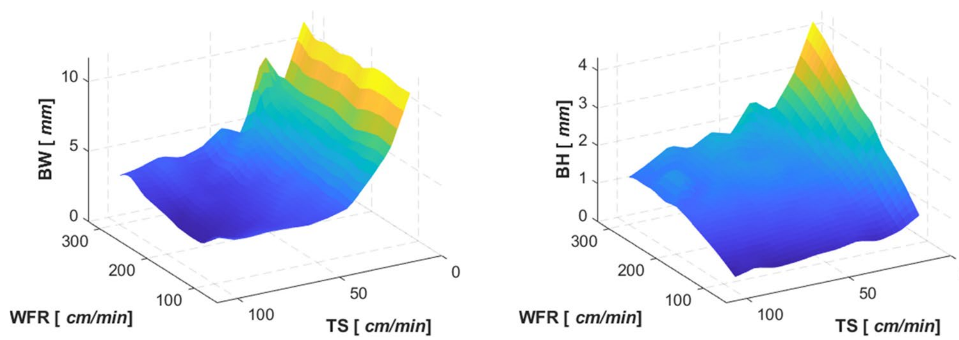

(a) (b)

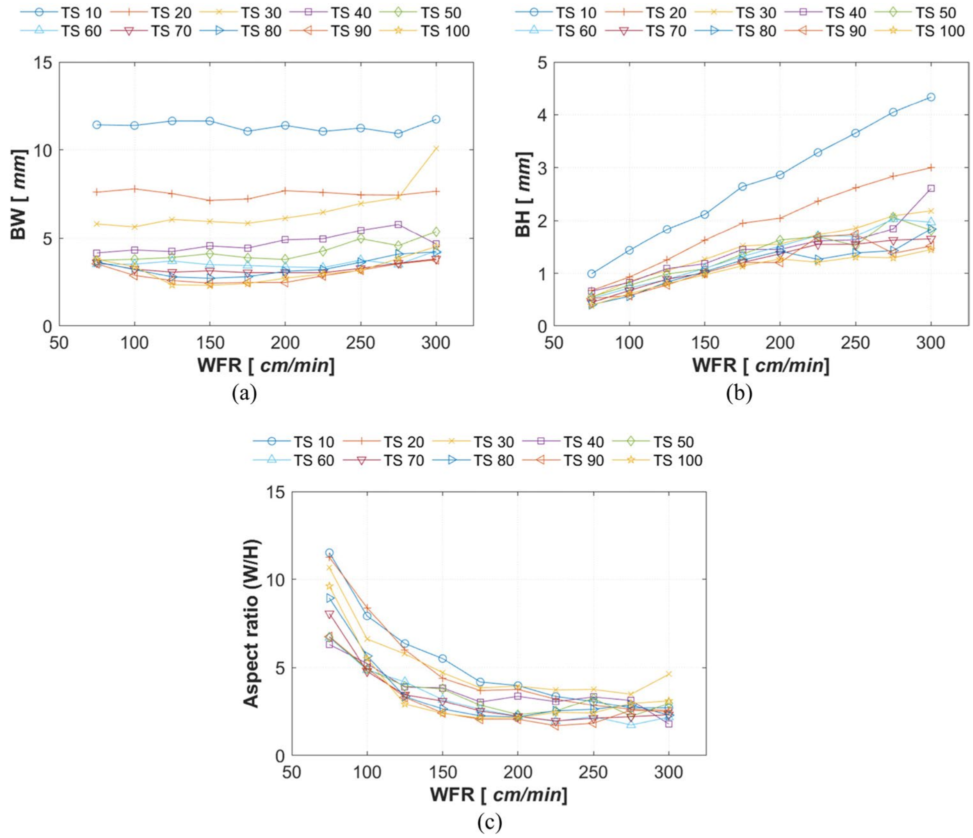

Fig. 20 Analysis of variance to display the effect of WFR on **a** bead width, **b** height, and **c** aspect ratio, in different TSs

are directly affected by the part properties [15]. During the WAAM processes, the signatures from process parameters have a high probability of not indicating the deterministic value that users set as a fixed value and can cause uncertainties. Therefore, the PS^2P^2 relation should be considered in experiment-based data-driven UQ.

4.4 Future research direction

The bead-on-plate study in this paper is based on the single-layer single bead. It can be a preliminary investigation of the mechanical properties of multi-layer deposited parts. The process parameters to make the near-optimal shape of the bead width and height on the single-layer single bead can be used in manufacturing multi-layer single or multi-beads. In these cases, the process is more complicated, leading to causing more uncertainties. The uncertainties generated from the single-layer single-bead case can be propagated and accumulated as the layers are stacked [83]. Accordingly, there are several issues in defect formation, microstructures, residual stress, and mechanical properties. In this subsection, we will discuss the mechanical property and residual stress in terms of uncertainty quantification and propagation. In addition, the digital twin-driven qualification for WAAM will be briefly discussed.

Process parameters can significantly affect the bead shape, defects, and microstructures. The bead shape affects the surface roughness in the WAAM part, while the defects (e.g., pore and crack) and microstructures affect the mechanical properties (e.g., hardness and tensile strength). Especially, for industrial applications, stringent requirements of mechanical properties in an additively manufactured part should be tested and satisfied. For this, the non-destructive evaluation (NDE) is highly demanding [84], since the destructive one is cost-intensive and time-consuming. However, the NDE knowledge for WAAM is significantly lacking, which is the main hindrance to its wide adoption in industry. Zhang et al. proposed a LSTM deep learning model for tensile strength prediction [85]. But, this model was developed for thermoplastic materials by destructive evaluation and did not investigate the uncertainties and its propagation. For the future work, the deep learning algorithms (e.g., a recurrent neural network focusing on LSTM) will be integrated with the proposed data-driven UQ framework for the process repeatability and part reproducibility in WAAM. By this, the data-driven UQ framework can expands its range from the bead geometry to the microstructure and mechanical properties of deposited parts with the NDE method.

The residual stress is developed by the non-equilibrium thermal cycles with the layer-by-layer stacking mechanism, resulting in distortion of the deposited part [34, 46]. The distortion is considered a defect that makes the parts achieve undesirable dimensional accuracy and mechanical properties [86]. To minimize the residual stress, several studies have been performed considering the different process parameters (e.g., heat inputs, interpass temperatures, and paths) [86–88]. However, the investigation of uncertainty quantification, propagation, and management of residual stress in WAAM is rare. Nath et al. proposed physics-informed computational models of residual stress and deformation with uncertainty consideration, but the models are based on fused filament fabrication [89]. For future work in WAAM, the proposed data-driven UQ framework will be extended for measuring, modeling, and validating the residual stress. For this, the uncertainties in residual stress need to be identified and quantified from the real process signatures in WAAM. For example, the residual stress and its uncertainty can be estimated and quantified with respect to various process parameters (e.g., wire feed rate, travel speed, and layer thickness). Process signatures (e.g., arc power and thermal data) can be used for relating the process parameters to the uncertainties.

WAAM also aims to manufacture parts ready to be employed as end-user products; therefore, producing defect-free parts is important. A digital twin (DT) technique can be developed using one or a combination of a mechanistic model, a sensing and control model, a statistical model, big data, or machine learning constructed virtually [90, 91]. The DTs of WAAM can provide process supervision, autonomous diagnostic process control, and process prediction [92]. They can extend the application of WAAM by achieving more repeatability in the processes, reproducibility in the deposited parts, and interoperability in the models [93]. Furthermore, the DT-driven qualification can save time and cost by minimizing trial and error, decreasing product defects, and reducing the product qualification path [82]. However, a generalized architecture of DT-driven qualification for WAAM has not been established yet. Future work will be the DT-driven qualification for WAAM by extending the proposed data-driven UQ framework.

5 Conclusion

The UQ of the WAAM process has been a notable research subject. Especially, the data-driven approach in UQ is still in its infancy because it is cost- and time-intensive. This paper discussed a data-driven UQ framework for the WAAM process, focusing on the experiment-based approach. The process parameters and real-time signatures during experiments of the WAAM are the uncertainty sources in the proposed framework. This work demonstrates that this approach can be successfully applied to the UQ study of the WAAM process using the IN625 wire and LCS substrate to reveal the variability of bead geometry caused by various uncertainty sources. GSA was carried out to show the sensitivity of the bead width and height to uncertainty sources, including WFR, TS, current, and voltage-related features. ANOVA was also performed in the case study, indicating that the bead width is negatively correlated with TS and that the bead height has a positive and negative correlation with WFR and TS, respectively. Since experiment-based process signatures were obtained during the WAAM process in real experiments, a PS^2P^2 relation was established. Moreover, the V&V was also performed using experiment-based data. The proposed framework can be extended to the UQ study of other WAAM processes, and it can be a basis for DT-driven qualification.

Author contribution Junhee Lee preprocessed the real experimental data of wire + arc additive manufacturing; constructed the models; carried out the uncertainty quantification, the global sensitivity analysis, and the analysis of variance; and wrote an original first draft of this paper. Sainand Jadhav conducted experiments on the gas-tungsten arc welding-based wire + arc additive manufacturing. Duck Bong Kim provided the real experimental data of wire + arc additive manufacturing, helped to organize the contents of the writing, and commented on the draft. Kwanghee Ko reviewed and edited the draft of the paper. All authors read and approved the final manuscript.

Funding This research was supported by the MSIT (Ministry of Science and ICT), Korea, under the High-Potential Individuals Global Training Program (2021–0-01566), supervised by the IITP (Institute of Information and Communications Technology Planning & Evaluation).

Data availability Not applicable.

Code availability Not applicable.

Declarations

Ethics approval The submitted work is original, complete, and has not been accepted/published elsewhere in any form or language.

Consent to participate Not applicable.

Consent for publication Not applicable.

Competing interests The authors declare no competing interests.

References

1. Tennøe S, Halnes G, Einevoll GT (2018) Uncertainpy: a Python toolbox for uncertainty quantification and sensitivity analysis in computational neuroscience. Front Neuroinformatics 12:49. https://doi.org/10.3389/fninf.2018.00049
2. Shridhar K, Laumann F, Liwicki M (2019) A comprehensive guide to bayesian convolutional neural network with variational inference. arXiv preprint arXiv:1901.02731. https://doi.org/10.48550/arXiv.1901.02731
3. Hu Z, Mahadevan S (2017) Uncertainty quantification and management in additive manufacturing: current status, needs,

and opportunities. Int J Adv Manuf Technol 93(5):2855–2874. https://doi.org/10.1007/s00170-017-0703-5
4. Hamdia KM, Msekh MA, Silani M, Vu-Bac N, Zhuang X, Nguyen-Thoi T, Rabczuk T (2015) Uncertainty quantification of the fracture properties of polymeric nanocomposites based on phase field modeling. Compos Struct 133:1177–1190. https://doi.org/10.1016/j.compstruct.2015.08.051
5. Nath P, Hu Z, Mahadevan S (2018) Modeling and uncertainty quantification of material properties in additive manufacturing. In: Proceedings of 2018 AIAA Non-Deterministic Approaches Conference. p 0923. https://doi.org/10.2514/6.2018-0923
6. Roy M, Wodo O (2020) Data-driven modeling of thermal history in additive manufacturing. Addit Manuf 32:101017. https://doi.org/10.1016/j.addma.2019.101017
7. Wang Z, Liu P, Hu Z, Chen L (2019) Simulation-based process optimization of metallic additive manufacturing under uncertainty. Int Des Eng Tech Conf Comput Inf Eng Conf 59186:V02AT03A030. https://doi.org/10.1115/DETC2019-97492
8. Kapusuzoglu B, Mahadevan S (2020) Physics-informed and hybrid machine learning in additive manufacturing: application to fused filament fabrication. Jom 72(12):4695–4705. https://doi.org/10.1007/s11837-020-04438-4
9. Guo M, Brune C (2021) Uncertainty quantification for physics-informed deep learning. In: Mathematics: Key Enabling Technology for Scientific Machine Learning. p 47–51.
10. Wang Z, Liu P, Ji Y, Mahadevan S, Horstemeyer MF, Hu Z, Chen L, Chen LQ (2019) Uncertainty quantification in metallic additive manufacturing through physics-informed data-driven modeling. Jom 71(8):2625–2634. https://doi.org/10.1007/s11837-019-03555-z
11. Wang Z, Liu P, Xiao Y, Cui X, Hu Z, Chen L (2019) A data-driven approach for process optimization of metallic additive manufacturing under uncertainty. J Manuf Sci Eng 141(8):081004. https://doi.org/10.1115/1.4043798
12. Zhang Y, Moon SK (2021) Data-driven design strategy in fused filament fabrication: status and opportunities. J Comput Des Eng 8(2):489–509. https://doi.org/10.1093/jcde/qwaa094
13. Mozaffar M, Paul A, Al-Bahrani R, Wolff S, Choudhary A, Agrawal A, Kornel E, Cao J (2018) Data-driven prediction of the high-dimensional thermal history in directed energy deposition processes via recurrent neural networks. Manuf Lett 18:35–39. https://doi.org/10.1016/j.mfglet.2018.10.002
14. Wang Z, Jiang C, Liu P, Yang W, Zhao Y, Horstemeyer M, Chen L, Hu Z, Chen L (2020) Uncertainty quantification and reduction in metal additive manufacturing. NPJ Comput Mater 6(1):1–10. https://doi.org/10.1038/s41524-020-00444-x
15 Hashemi SM, Parvizi S, Baghbanijavid H, Tan AT, Nematollahi M, Ramazani A, Fang N, Elahinia M (2022) Computational modelling of process–structure–property–performance relationships in metal additive manufacturing: a review. Int Mater Rev 67(1):1–46. https://doi.org/10.1080/09506608.2020.1868889
16. Lee SH (2020) Optimization of cold metal transfer-based wire arc additive manufacturing processes using gaussian process regression. Metals 10(4):461. https://doi.org/10.3390/met10040461
17. Barnes J, Kingsbury A, Bono E (2016) Does low cost titanium powder yield low cost titanium parts. In: Proceedings of PowderMet 2016 international conference on powder metallurgy. Boston, MA
18. Kim DB, Witherell P, Lu Y, Feng S (2017) Toward a digital thread and data package for metals-additive manufacturing. Smart Sustain Manuf Syst 1(1):75. https://doi.org/10.1520/SSMS20160003
19. Seo G, Ahsan MR, Lee Y, Shin JH, Park H, Kim DB (2021) A functional modeling approach for quality assurance in metal additive manufacturing. Rapid Prototyp J 27(2):288–303. https://doi.org/10.1108/RPJ-12-2018-0312
20. Olson GB (1997) Computational design of hierarchically structured materials. Science 277(5330):1237–1242. https://doi.org/10.1126/science.277.5330.1237
21. Olson GB (2001) Brains of steel: mind melding with materials. Int J Eng Educ 17(4/5):468–471
22. McDowell DL, Olson GB (2008) Concurrent design of hierarchical materials and structures. In: Yip S, Rubia T (eds) Scientific modeling and simulations. Springer, Dordrecht, pp 207–240
23. Huang DJ, Li H (2021) A machine learning guided investigation of quality repeatability in metal laser powder bed fusion additive manufacturing. Mater Des 203:109606. https://doi.org/10.1016/j.matdes.2021.109606
24. Lopez F, Witherell P, Lane B (2016) Identifying uncertainty in laser powder bed fusion additive manufacturing models. J Mech Des 138(11):114502. https://doi.org/10.1115/1.4034103
25. Tang S, Wang G, Song H, Li R, Zhang H (2021) A novel method of bead modeling and control for wire and arc additive manufacturing. Rapid Prototyp J 27:311–320. https://doi.org/10.1108/RPJ-05-2020-0097
26. Kats D, Wang Z, Gan Z, Liu WK, Wagner GJ, Lian Y (2022) A physics-informed machine learning method for predicting grain structure characteristics in directed energy deposition. Comput Mater Sci 202:110958. https://doi.org/10.1016/j.commatsci.2021.110958
27. Mondal B, Mukherjee T, DebRoy T (2022) Crack free metal printing using physics informed machine learning. Acta Mater 226:117612. https://doi.org/10.1016/j.actamat.2021.117612
28. Schwalbach EJ, Donegan SP, Chapman MG, Chaput KJ, Groeber MA (2019) A discrete source model of powder bed fusion additive manufacturing thermal history. Addit Manuf 25:485–498. https://doi.org/10.1016/j.addma.2018.12.004
29. Singh SR, Khanna P (2021) Wire arc addtivie menufacturing (WAAM): A new process to shape engineering materials. Mater Today: Proc 44:118–128. https://doi.org/10.1016/j.matpr.2020.08.030
30. Rosli NA, Alkahari MR, Bin Abdollah MF, Maidin S, Ramli FR, Herawan SG (2021) Review on effect of heat input for wire arc additive manufacturing process. J Mater Res Technol 11:2127–2145. https://doi.org/10.1016/j.jmrt.2021.02.002
31. Ding D, Pan Z, Cuiuri D, Li H, Van Duin S, Larkin N (2016) Bead modelling and implementation of adaptive MAT path in wire and arc additive manufacturing. Robot Comput-Integr Manuf 39:32–42. https://doi.org/10.1016/j.rcim.2015.12.004
32. Ding D, Pan Z, Cuiuri D, Li H, Larkin N (2016) Adaptive path planning for wire-feed additive manufacturing using medial axis transformation. J Clean Prod 133:942–952. https://doi.org/10.1016/j.jclepro.2016.06.036
33. Ding D, Pan Z, Dominic C, Li H (2015) A practical path planning methodology for wire and arc additive manufacturing of thin-walled structures. Robot Comput-Integr Manuf 34:8–19. https://doi.org/10.1016/j.rcim.2015.01.003
34. Ding D, Pan Z, Cuiuri D, Li H (2015) Wire-feed additive manufacturing of metal components: technologies, developments and future interests. Int J Adv Manuf Technol 81:465–481. https://doi.org/10.1007/s00170-015-7077-3
35. Tanvir M, Ahsan R, Ji C, Hawkins W, Bates B, Kim D (2019) Heat treatment effects on Inconel 625 components fabricated by wire+arc additive manufacturing (WAAM)—part 1: microstructural characterization. Int J Adv Manuf Technol 103(9):3785–3798. https://doi.org/10.1007/s00170-019-03828-6
36. Lee C, Seo G, Kim D, Kim M, Shin J (2021) Development of defect detection AI model for wire+ arc additive manufacturing using high dynamic range images. Appl Sci 11(16):7541. https://doi.org/10.3390/app11167541
37. Cho HW, Shin SJ, Seo GJ, Kim DB, Lee DH (2022) Real-time anomaly detection using convolutional neural network in wire arc additive manufacturing: molybdenum material. J Mater Process

Technol 302:117495. https://doi.org/10.1016/j.jmatprotec.2022.117495
38. Nath P, Hu Z, Mahadevan S (2017) Mutli-level uncertainty quantification in additive manufacturing. In: Proceedings of 2017 International Solid Freeform Fabrication Symposium, University of Texas at Austin. p 922–937. https://hdl.handle.net/2152/89891
39. Hu Z, Mahadevan S (2017) Uncertainty quantification in prediction of material properties during additive manufacturing. Scripta Mater 135:135–140. https://doi.org/10.1016/j.scriptamat.2016.10.014
40. Tian C, Li T, Bustillos J, Bhattacharya S, Turnham T, Yeo J, Moridi A (2021) Data-driven approaches toward smarter additive manufacturing. Adv Intell Syst 3(12):2100014. https://doi.org/10.1002/aisy.202100014
41. Ding D, Pan Z, Cuiuri D, Li H (2015) A multi-bead overlapping model for robotic wire and arc additive manufacturing (WAAM). Robot Comput-Integr Manuf 31:101–110. https://doi.org/10.1016/j.rcim.2014.08.008
42. Li Y, Sun Y, Han Q, Zhang G, Horváth I (2018) Enhanced beads overlapping model for wire and arc additive manufacturing of multi-layer multi-bead metallic parts. J Mater Process Technol 252:838–848. https://doi.org/10.1016/j.jmatprotec.2017.10.017
43. Lambiase F, Scipioni SI, Paoletti A (2022) Accurate prediction of the bead geometry in wire arc additive manufacturing process. Int J Adv Manuf Technol 119:7629–7639. https://doi.org/10.1007/s00170-021-08588-w
44. Veiga F, Suarez A, Aldalur E, Artaza T (2022) Wire arc additive manufacturing of invar parts: Bead geometry and melt pool monitoring. Measurement 189:110452. https://doi.org/10.1016/j.measurement.2021.110452
45. Xue Q, Ma S, Liang Y, Wang J, Wang Y, He F, Liu M (2018) Weld bead geometry prediction of additive manufacturing based on neural network. In: Proceedings of 2018 11th International Symposium on Computational Intelligence and Design. p 47–51. https://doi.org/10.1109/ISCID.2018.10112
46. Dinovitzer M, Chen X, Laliberte J, Huang X, Frei H (2019) Effect of wire and arc additive manufacturing (WAAM) process parameters on bead geometry and microstructure. Addit Manuf 26:138–146. https://doi.org/10.1016/j.addma.2018.12.013
47. Cho J, Lee D, Seo G, Kim D, Shin S (2022) Optimizing the mean and variance of bead geometry in the wire+arc additive manufacturing using a desirability function method. Int J Adv Manuf Technol 120:7771–7783. https://doi.org/10.1007/s00170-022-09237-6
48. Frazier WE (2014) Metal additive manufacturing: a review. J Mater Eng Perform 23(6):1917–1928. https://doi.org/10.1007/s11665-014-0958-z
49. Lewandowski JJ, Seifi M (2016) Metal additive manufacturing: a review of mechanical properties. Annu Rev Mater Res 46:151–186. https://doi.org/10.1146/annurev-matsci-070115-032024
50. Xia C, Pan Z, Polden J, Li H, Xu Y, Chen S (2022) Modeling and prediction of surface roughness in wire arc additive manufacturing using machine learning. J Intell Manuf 33:1467–1482. https://doi.org/10.1007/s10845-020-01725-4
51. Xiong J, Li Y, Li R, Yin Z (2018) Influences of process parameters on surface roughness of multi-layer single-pass thin-walled parts in GMAW-based additive manufacturing. J Mater Process Technol 252:128–136. https://doi.org/10.1016/j.jmatprotec.2017.09.020
52. Yildiz A, Davut K, Koc B, Yilmaz O (2020) Wire arc additive manufacturing of high-strength low alloy steels: study of process parameters and their influence on the bead geometry and mechanical characteristics. Int J Adv Manuf Technol 108:3391–3404. https://doi.org/10.1007/s00170-020-05482-9
53. Elsokaty A, Oraby O, Sadek S, Salem H (2023) Influence of wire arc additive manufacturing beads' geometry and building strategy: mechanical and structural behavior of ER70S-6 prismatic blocks. J Manuf Mater Process 7:3. https://doi.org/10.3390/jmmp7010003
54. Hauser T, Reisch R, Breese P, Lutz B, Pantano M, Nalam Y, Bela K, Kamps T, Volpp J, Kaplan A (2021) Porosity in wire arc additive manufacturing of aluminium alloys. Addit Manuf 41:101993. https://doi.org/10.1016/j.addma.2021.101993
55. Wang Z, Yang W, Liu Q, Zhao Y, Liu P, Wu D, Mihaela B, Chen L (2022) Data-driven modeling of 2.2 and property in additive manufacturing: a review and future directions. J Manuf Process 77:13–31. https://doi.org/10.1016/j.jmapro.2022.02.053
56. Yang XS (2020) Nature-inspired optimization algorithms. Academic Press
57 Chau T, Burovskiy P, Flynn M, Luk W (2017) Advances in dataflow systems. In A. Hurson, V. Milutinović (Eds.). Adv Comput 106:21–62. https://doi.org/10.1016/bs.adcom.2017.04.002. (Elsevier)
58. Oh Y, Sharp M, Sprock T, Kwon S (2021) Neural network-based build time estimation for additive manufacturing: a performance comparison. J Comput Des Eng 8(5):1243–1256. https://doi.org/10.1093/jcde/qwab044
59. Francis J, Bian L (2019) Deep learning for distortion prediction in laser-based additive manufacturing using big data. Manuf Lett 20:10–14. https://doi.org/10.1016/j.mfglet.2019.02.001
60. Chen YC (2017) A tutorial on kernel density estimation and recent advances. Biostat Epidemiol 1(1):161–187. https://doi.org/10.1080/24709360.2017.1396742
61. Gramacki A (2018) Nonparametric kernel density estimation and its computational aspects, vol 37. Springer International Publishing, Cham
62. Malato G (2021) How to calculate confidence intervals in Python. https://towardsdatascience.com/how-to-calculate-confidence-intervals-in-python-a8625a48e62b. Accessed 7 June 2022
63. Saksh (2021) Calculate confidence interval in Python (with examples). https://vedexcel.com/how-to-calculate-confidence-intervals-in-python/. Accessed 7 June 2022
64. Liang B (2010) Error and uncertainty quantification and sensitivity analysis in mechanics computational models. MS dissertation. Vanderbilt University, Nashville
65. Liang B, Mahadevan S (2011) Error and uncertainty quantification and sensitivity analysis in mechanics computational models. Int J Uncertain Quantif 1(2):147–161. https://doi.org/10.1615/Int.J.UncertaintyQuantification.v1.i2.30
66. Sobol IM (1993) Sensitivity analysis for non-linear mathematical models. Math Model Comput Exp 1:407–414
67. Archer GEB, Saltelli A, Sobol IM (1997) Sensitivity measures, ANOVA-like techniques and the use of bootstrap. J Stat Comput Simul 58(2):99–120. https://doi.org/10.1080/00949659708811825
68 Saltelli A, Annoni P, Azzini I, Campolongo F, Ratto M, Tarantola S (2010) Variance based sensitivity analysis of model output. Design and estimator for the total sensitivity index. Comput Phys Commun 181(2):259–270. https://doi.org/10.1016/j.cpc.2009.09.018
69. Sobol IM (2001) Global sensitivity indices for nonlinear mathematical models and their Monte Carlo estimates. Math Comput Simul 55(1–3):271–280. https://doi.org/10.1016/S0378-4754(00)00270-6
70. Oberkampf WL, Roy CJ (2010) Verification and validation in scientific computing. Cambridge University Press
71. Oden T, Moser R, Ghattas O (2010) Computer predictions with quantified uncertainty, part I. SIAM News 43(9):1–3
72. Riedmaier S, Danquah B, Schick B, Diermeyer F (2021) Unified framework and survey for model verification, validation and uncertainty quantification. Arch Comput Methods Eng 28(4):2655–2688. https://doi.org/10.1007/s11831-020-09473-7
73. Flood A, Liou F (2018) Review of metal AM simulation validation techniques. J Mech Eng Autom 8:43–52. https://doi.org/10.17265/2159-5275/2018.02.001

74. Geng H, Xiong J, Huang D, Lin X, Li J (2017) A prediction model of layer geometrical size in wire and arc additive manufacture using response surface methodology. Int J Adv Manuf Technol 93(1):175–186. https://doi.org/10.1007/s00170-015-8147-2
75. Kim J, Seo G, Kim D, Shin J, Park H (2021) Machine learning models for detecting weld bead defects in wire-arc additive manufacturing. Korean J Comput Des Eng 26(2):131–143. https://doi.org/10.7315/CDE.2021.131
76. Hexagon (2022) PC-DMIS. https://www.hexagonmi.com/products/software/pc-dmis. Accessed 7 June 2022
77. CloudCompare (2022) 3D point cloud and mesh processing software. https://www.danielgm.net/cc/. Accessed 7 June 2022
78. Xiong J, Zhang G, Hu J, Wu L (2014) Bead geometry prediction for robotic GMAW-based rapid manufacturing through a neural network and a second-order regression analysis. J Intell Manuf 25:157–163. https://doi.org/10.1007/s10845-012-0682-1
79. Ding D, Shen C, Pan Z, Cuiuri D, Li H, Larkin N, Duin S (2016) Towards an automated robotic arc-welding-based additive manufacturing system from CAD to finished part. Comput Aided Des 73:66–75. https://doi.org/10.1016/j.cad.2015.12.003
80 Herman J, Usher W (2017) SALib: an open-source Python library for sensitivity analysis. J Open Source Softw 2(9):97. https://doi.org/10.21105/joss.00097
81. Debroy T, Zhang W, Turner J, Babu SS (2017) Building digital twins of 3D printing machines. Scripta Mater 135:119–124. https://doi.org/10.1016/j.scriptamat.2016.12.005
82. Hussein RO, Nie X, Northwood DO (2013) Processing-structure-properties-performance relationships for Mg-alloys coated using plasma electrolytic oxidation (PEO) Method. In: Material Forum, Vol 37
83. Mahadevan S, Nath P, Hu Z (2022) Uncertainty quantification for additive manufacturing process improvement: recent advances. ASCE-ASME J Risk Uncertain Eng Syst, Part B: Mech Eng 8:010801. https://doi.org/10.1115/1.4053184
84. Srivastava M, Rathee S, Tiwaru A, Dongre M (2023) Wire arc additive manufacturing of metals: a review on processes, materials and their behavior. Mater Chem Phys 294:126988. https://doi.org/10.1016/j.matchemphys.2022.126988
85. Zhang J, Wang P, Gao R (2019) Deep learning-based tensile strength prediction in fused deposition modeling. Comput Ind 107:11–21. https://doi.org/10.1016/j.compind.2019.01.011
86. Hönnige J, Seow C, Ganguly S, Xu X, Cabeza S, Coules H, Williams S (2021) Study of residual stress and microstructural evolution in as-deposited and inter-pass rolled wire plus arc additively manufactured Inconel 718 alloy after ageing treatment. Mater Sci Eng: A 801:140368. https://doi.org/10.1016/j.msea.2020.140368
87. Jafari D, Vaneker T, Gibson I (2021) Wire and arc additive manufacturing: opportunities and challenges to control the quality and accuracy of manufactured parts. Mater Des 202:109471. https://doi.org/10.1016/j.matdes.2021.109471
88. Chen S, Gao H, Zhang Y, Wu Q, Gao Z, Zhou X (2022) Review on residual stresses in metal additive manufacturing: formation mechanisms, parameter dependencies, prediction and control approaches. J Market Res 17:2950–2974. https://doi.org/10.1016/j.jmrt.2022.02.054
89. Nath P, Olson J, Mahadevan S, Lee Y (2020) Optimization of fused filament fabrication process parameters under uncertainty to maximize part geometry accuracy. Addit Manuf 35:101331. https://doi.org/10.1016/j.addma.2020.101331
90. Knapp GL, Mukherjee T, Zuback JS, Wei HL, Palmer TA, De A, DebRoy T (2017) Building blocks for a digital twin of additive manufacturing. Acta Mater 135:390–399. https://doi.org/10.1016/j.actamat.2017.06.039
91. Mukherjee T, DebRoy T (2019) A digital twin for rapid qualification of 3D printed metallic components. Appl Mater Today 14:59–65. https://doi.org/10.1016/j.apmt.2018.11.003
92. Gunasegaram DR, Murphy AB, Matthews MJ, DebRoy T (2021) The case for digital twins in metal additive manufacturing. J Phys: Mater 4(4):040401. https://doi.org/10.1088/2515-7639/ac09fb
93. Kim D, Shao G, Jo G (2022) A digital twin implementation architecture for wire + arc additive manufacturing based on ISO 23247. Manuf Lett 34:1–5. https://doi.org/10.1016/j.mfglet.2022.08.008